Performance of rotation-symmetric bosonic codes in the presence of non-Markovian effects induced by random telegraph noise

Performance of rotation-symmetric bosonic codes in the presence of non-Markovian effects induced by random telegraph noise

Adithi Udupa,[1,*] Timo Hillmann,[1] Rabsan Galib Ahmed,[2] Andrea Smirne,[3,4] and Giulia Ferrini[1,†]

[1]*Department of Microtechnology and Nanoscience, Chalmers University of Technology, SE-412 96 Göteborg, Sweden*

[2]*Department of Physical Sciences, Indian Institute of Science Education and Research Mohali, Mohali, Punjab 140306, India*

[3]*Department of Physics, University of Milan, I-20122 Milan, Italy*

[4]*Istituto Nazionale di Fisica Nucleare, Sezione di Milano, Via Celoria 16, I-20133 Milan, Italy*

(Received 11 July 2025; accepted 6 March 2026; published 2 April 2026)

Decoherence in quantum devices, such as qubits and resonators, is often caused by bistable fluctuators modeled as random telegraph noise (RTN), leading to significant dephasing. We analyze the impact of individual and multiple fluctuators on a bosonic mode in continuous variable systems, identifying non-Markovian behavior governed by two timescales: the switching rate (ξ) and the coupling strength (ν) of the fluctuator. Using the Breuer-Laine-Piilo trace-distance measure, we characterize non-Markovianity for both Gaussian and non-Gaussian states, revealing that for rotation-symmetric bosonic (RSB) codes, known for their error-correction advantages, the measure grows linearly with code symmetry and can become unbounded. We evaluate the performance of these RSB codes under simultaneous loss and RTN dephasing. For a teleportation-based Knill error-correction circuit, the codes perform robustly in the Markovian limit. In the non-Markovian regime, the performance depends nontrivially on the time at which the error correction is performed. The average gate fidelity of the error-corrected state in this case exhibits oscillations as a function of time due to the oscillatory nature of the dephasing function of the RTN noise; however, for most of the parameter ranges, the values stay beyond the breakeven point. Extending to multiple fluctuators that produce $1/f$ noise, we observe that non-Markovianity decays with increasing fluctuator count, while the performance of RSB codes remains effective with increasing number of fluctuators.

DOI: 10.1103/xfv4-8dq7

I. INTRODUCTION

Bosonic codes are promising for hardware-efficient quantum error-correction (QEC) protocols and hold thereby significant potential for achieving fault-tolerant quantum computation [1–11] with reduced overheads. Implementations of bosonic codes for Quantum Error Correction have been achieved with superconducting microwave circuits [12–18], trapped ions [19–22], and on photonic platforms [9,23].

Along with photon or phonon losses, one of the main sources of noise in bosonic systems, and in some cases the dominating one [19], is (photon number) dephasing. For dephasing type of noise, bosonic codes with a discrete rotational symmetry in phase space are particularly suitable and yield good performance in terms of the capability of restoring the intended quantum information [24–26], due to phase space structure of the code words, i.e., the bosonic states that encode the logical qubit states $|0\rangle$ and $|1\rangle$ [27].

So far, the performance of rotation-symmetric bosonic (RSB) under dephasing noise has been studied only for the simplest case of Gaussian, Markovian dephasing [25,26,28]. However, in several experimental platforms, other types of noise arise. For instance, microwave cavities coupled to superconducting qubits are affected by decoherence effects stemming from the coupling with one or more random fluctuators present on the sample substrate [29–34]. These fluctuators are often modeled in terms of two-level systems (TLSs) [35–38] switching between two metastable states at random intervals and yielding a random telegraph noise (RTN) [39,40]. The dynamics of a state coupled to such a TLS with an average switching rate ξ and coupling strength ν undergoes a transition from a Markovian to a non-Markovian evolution depending on the ratio of the two timescales, $r = \xi/\nu$. RTN is also often associated with a colored noise with characteristic $1/f$ power spectrum [41,42]. This is modeled by either using a distribution of switching rates for a single RTN fluctuator or by coupling multiple independent fluctuators to the system with different switching rates.

The performance of bosonic codes under these types of noise has not yet been studied; indeed, while error correction under non-Markovian noise has been studied for qubits [43,44], it remains largely unexplored for bosonic systems. Furthermore, so far, the study of non-Markovianity in bosonic systems from an open quantum system perspective, e.g., when it comes to quantifying non-Markovianity with suitable measures, has been limited to the case of Gaussian states and Gaussian channels [45,46].

In this work, we address both gaps. First, we characterize the non-Markovianity arising in a bosonic mode coupled

*Contact author: adithi@chalmers.se

†Contact author: ferrini@chalmers.se

to non-Gaussian classical environments corresponding to the two types of noise described above by evaluating the trace distance between two initial states [47,48] for the case of rotationally symmetric bosonic code words, which are a subset of non-Gaussian states. We show that the resulting non-Markovianity measure exceeds the one obtained for the case of Gaussian states and that it increases linearly with the order of RSB code symmetry, suggesting that it is unbounded.

Second, we study the performance of RSB under RTN and colored noise with a $1/f$ spectrum for the case of a realistic state recovery procedure. The state recovery procedure that we consider is based on the Knill teleportation scheme, and its constituent circuit elements are readily available in photonics and superconducting laboratories [25,27]. In the Markovian limit of the RTN, the RSB codes are found to perform well, agreeing with the previous results in Refs. [25,27], including the case where dephasing is combined with a loss channel. In the non-Markovian limit, we see that the performance depends on the time at which error correction happens, with certain timescales giving a significant improvement in fidelities compared to the breakeven potential, the threshold where the lifetime of the error-corrected qubit is as good as that of an unencoded qubit. We show that the span of these desirable time intervals can be further increased by tuning the parameters of the RSB codes. For a given time, however, the performance degrades close to the transition between the two regimes.

Our results have therefore implications both for identifying codes and parameter regimes yielding the most effective quantum error correction in the presence of non-Markovian dephasing and for understanding and characterizing such types of noise from an open quantum system perspective.

The structure of the rest of the paper is as follows: Section II introduces the noise models, provides a detailed analysis of evolution of a bosonic mode under RTN and $1/f$ noise models, and presents simulations and analytical calculations for the dynamics of the state of a bosonic mode under such noises, in both Markovian and non-Markovian regimes. In Sec. III, we introduce the concept of non-Markovianity using the trace-distance measure and assess the non-Markovianity measure for Gaussian states and rotation-symmetric bosonic states, respectively, in the presence of RTN. Finally, in Sec. IV, we analyze the performance of rotation-symmetric bosonic codes such as cat and binomial codes under a Knill error-correction (Knill EC) circuit, with the input states subjected to loss and RTN dephasing or $1/f$ noise. All the numerical calculations have been performed using the QuTip package [49,50]. Appendixes A–K address various technical derivations and additional results on the characterization of non-Markovianity and performance of binomial codes in the presence of these noise models.

Table I provides a summary of the abbreviations used in this work. We now proceed further to an extensive characterization of RTN and $1/f$ noises in bosonic systems.

TABLE I. List of abbreviations.

Abbreviation	Definition
CV	Continuous variable
QEC	Quantum Error Correction
RTN	Random Telegraph Noise
BLP	Breuer-Laine-Piilo
RSB	Rotation-Symmetric Bosonic
Knill EC	Knill error correction
TLS	Two-Level System

II. STATE EVOLUTION UNDER RANDOM TELEGRAPH NOISE AND $1/f$ NOISE

In the realization of solid-state qubits and superconducting microwave resonators, the primary intrinsic noise arises from fluctuations due to TLSs. These TLSs may result from tunneling atoms, dangling electronic bonds, impurity atoms, trapped charge states, and similar sources [35–38]. This noise can be attributed to a single strongly coupled fluctuator or a set of a few fluctuators with a distribution of hopping rates, generating $1/f$ noise. Such environments are often modeled by one or more fluctuators interacting with a bosonic bath, typically consisting of phonons or electron-hole pairs. The interaction between the fluctuators and the environment manifests as time-dependent random fields that affect the system, behaving as stochastic noise that can be treated classically [38]. In this section, we first investigate a bosonic mode coupled with a single fluctuator. We then analyze the non-Markovian signatures from the random telegraph noise for Gaussian and non-Gaussian states. We finally extend the study to a more generalized case of $1/f$ noise arising from either a single fluctuator with varying switching rates or from multiple fluctuators coupled to the bosonic mode.

A. Hamiltonian and state evolution for RTN noise

We first consider a bosonic mode coupled with strength ν to a single fluctuator that has an average switching rate ξ, resulting in random telegraphlike noise. As we will show, the coupling strength ν and the switching rate ξ are the two critical timescales that determine the system's non-Markovianity. Let $c(t)$ represent the function that characterizes the fluctuator's state at time t, with value ± 1 following the statistical properties of the RTN. This noise is further characterized by an exponentially decaying autocorrelation function and has a Lorentzian power spectrum. The Hamiltonian for the bosonic mode coupled to the time-dependent fluctuating field is given by [35,38,51,52]

$$\hat{H}_{\mathrm{RTN}} = \epsilon \hat{a}^\dagger \hat{a} + \nu c(t) \hat{a}^\dagger \hat{a}, \tag{1}$$

where ϵ is the energy level of the bosonic mode, and $\hat{a}$, $\hat{a}^\dagger$ are, respectively, the annihilation and creation operators for the bosonic mode. The coupling strength of the bosonic mode to the field is given by ν. We define the quantity r to be the ratio of the two timescales ξ and ν, that is $r = \xi/\nu$. This interaction describes a nondissipative dephasing channel, suitable for modeling environments where dephasing is the dominant decoherence mechanism. The effects of this type of noise have been well studied so far on qubits [53–57]. For a qubit coupled to a fluctuator, it has been shown that in the regime $r > 1$, the dynamics is Markovian, while for $r < 1$, the system exhibits non-Markovianity. Going back to our bosonic-mode system and further introducing two dimensionless quantities $\tau = \nu t$ and $r = \xi/\nu$, we obtain the expression for the evolved density

matrix as

$$\hat{\rho}_{\rm RTN}(\tau) = \sum_{m,n=0}^{\infty} \langle e^{i\phi_{\rm RTN}(\tau)(m-n)}\rangle_{\phi_{\rm RTN}(\tau)} \rho_{m,n} |m\rangle\langle n|, \quad (2)$$

where $\phi_{\rm RTN}(\tau) = \int_0^\tau c(\tau')d\tau'$. The averaging $\langle\cdots\rangle_{\phi_{\rm RTN}(t)}$ is performed over different instances of the random telegraph stochastic noise. The quantity $\langle e^{i\phi_{\rm RTN}(\tau)(m-n)}\rangle_{\phi_{\rm RTN}(t)}$ is called the dephasing function $G(r,\tau)$ and reads

$$\langle e^{i\phi_{\rm RTN}(\tau)(m-n)}\rangle_{\phi_{\rm RTN}(\tau)} = e^{-r\tau}\left(\cosh\Omega\tau + \frac{r}{\Omega}\sinh\Omega\tau\right), \quad (3)$$

where $\Omega = \sqrt{r^2-(m-n)^2}$. The complete derivation for the evolved density matrix is provided in Appendix A. This expression shows that, in addition to the ratio r, the dephasing function depends on the support of the state in the Fock basis, leading to either oscillatory or decaying behavior with time, depending on the given state.

B. Hamiltonian and state evolution for $1/f$ noise

To consider the impact of the interaction with more RTN fluctuators, we need to specify their spectral density. In numerous physical systems, the noise spectral density exhibits a $1/f$ dependence across a wide frequency range. This characteristic low-frequency behavior is observed in diverse systems, including bulk semiconductors, normal and superconducting metals, strongly disordered conductors, and devices fabricated from these materials [58–60]. The simplest and most widely adopted model for describing $1/f$ noise involves a distribution of switching rates of single RTN fluctuators. If the switching rates within a given range have a distribution that is proportional to the inverse of the switching rate, then the power spectral density follows the behavior, $S(\omega) \propto 1/\omega$ [41].

In the remainder of the paper, we consider a bosonic mode coupled to a fixed number of RTN fluctuators N_f, with the Hamiltonian given by [57]

$$\hat{H}_{1/f} = \epsilon\hat{a}^\dagger\hat{a} + \frac{\nu}{\sqrt{N_f}}\sum_{i=1}^{N_f} c_i(t)\hat{a}^\dagger\hat{a}, \quad (4)$$

where the ith fluctuator has a switching rate ξ_i.

With a similar change of variables $\tau = \nu t$ and $r = \xi/\nu$, for a general bosonic state, the evolved density matrix can be written as

$$\hat{\rho}_{1/f}(\tau) = \sum_{m,n=0}^{\infty} \langle e^{i\Phi_{1/f}(\tau)(m-n)}\rangle_{\Phi_{1/f}(\tau)} \rho_{m,n} |m\rangle\langle n|. \quad (5)$$

Here, $\Phi_{1/f}(\tau) = \frac{1}{\sqrt{N_f}}\sum_i \phi_{i,\rm RTN}(\tau)$, where $\phi_{i,\rm RTN}(\tau) = \int_0^\tau d\tau' c_i(\tau')$. The averaging operation $\langle\cdot\rangle_{\Phi_{1/f}(\tau)}$ can be computed explicitly as follows:

$$\begin{aligned}\langle e^{i\sum_i \phi_{i,\rm RTN}(\tau)(m-n)}\rangle_{\Phi_{1/f}(\tau)} &= \langle e^{i\phi_{1,\rm RTN}(\tau)(m-n)} e^{i\phi_{2,\rm RTN}(\tau)(m-n)}\cdots\rangle \\ &= (\overline{\langle e^{i\phi_{\rm RTN}(\tau)(m-n)}\rangle})^{N_f}, \end{aligned} \quad (6)$$

where the first averaging $\langle\cdots\rangle_{\phi_{\rm RTN}(\tau)}$ is over different instances of the RTN as before, the second averaging operation $\overline{\langle\cdots\rangle}$ is performed over the distribution of switching rates of the fluctuators. Using the form of the distribution, the quantity $\langle e^{i\sum_i \phi_{i,\rm RTN}(\tau)(m-n)}\rangle$ can be converted to an integral, and its analytical evaluation has been done in Appendix B.

C. Simulation and analytical results for the dynamics of a coherent state

Before investigating the presence of non-Markovian effects for the above two cases, we explore the evolution of the Wigner function [61] of the bosonic mode. This is crucial for the understanding of the behavior of non-Markovianity of different bosonic codes as well the performance of these codes as we will see in the later sections. The Wigner function of a single-mode bosonic mode $\hat{\rho}$ is given by

$$W(q,p) = \frac{1}{2\pi}\int {\rm d}x\, e^{-ipx}\left\langle q+\frac{x}{2}\middle|\hat{\rho}\middle|q-\frac{x}{2}\right\rangle \quad (7)$$

defined over the phase space $(q,p)\in\mathbb{R}^2$. In Fig. 1, we plot evolution of the Wigner function for a coherent state with amplitude $\alpha = 4$ under RTN dephasing with different values of r [Figs. 1(a)–1(c)], for the case of Gaussian dephasing [Fig. 1(d)] and for $1/f$ noise for $N_f = 2, 10$ [Figs. 1(e) and 1(f)]. For RTN dephasing with smaller values of r, the dominant contribution to the density matrix at early times comes from two "bloblike" structures that rotate in opposite directions in the phase space and that eventually dephase completely at longer times. As r increases, the contribution of states between the blobs becomes larger, and the state dephases over a shorter timescale. In Fig. 1(d), we show the evolution of the same coherent state under a Gaussian dephasing channel. A Gaussian dephasing channel is described by its action on an initial state $\hat{\rho}_0$ as $\mathcal{N}_{\sigma^2}\hat{\rho}_0 = \int_{-\infty}^{\infty} d\phi\, p(\phi) e^{-i\phi\hat{n}}\hat{\rho}_0 e^{i\phi\hat{n}}$, with dephasing angles ϕ drawn from a Gaussian distribution with variance $\sigma^2 = k_\phi\tau$, where $k_\phi = k'_\phi/\nu$ and k'_ϕ is the rate of dephasing. The results suggest that as the switching rate of the RTN noise increases, the noise behavior tends to approach the Gaussian (Markovian) limit. This observation is consistent with the understanding that at higher switching rates and longer times, the RTN behaves increasingly like a Markovian channel. In Figs. 1(e) and 1(f), we show the evolution of the same state under $1/f$ noise with the range of r going from $r_{\rm min} = 10^{-4}$ to $r_{\rm max} = 10^4$ taken from experimental relevant values [29,32]. For two fluctuators, the evolution of the Wigner function has bloblike behavior showing signs of non-Markovianity; however, for a large number of fluctuators, the evolution once again becomes similar to that of the Gaussian dephasing case [panel (d)].

We now analyze the results of RTN dephasing analytically in both the small- and large-r regimes. From Eq. (2), when $r \ll 1$ and on shorter timescales, the formation of the blobs can be understood as follows. Consider the initial state to be a coherent state $|\alpha\rangle$ with $\alpha = \alpha_0 e^{i\theta}$, and the initial density matrix $\hat{\rho}_0 = |\alpha_0,\theta\rangle\langle\alpha_0,\theta|$. The expression for the density matrix in the zeroth order of r and τ becomes (see Appendix C)

$$\hat{\rho}(\tau) = \tfrac{1}{2}|\alpha_0,\theta+\tau\rangle\langle\alpha_0,\theta+\tau| + \tfrac{1}{2}|\alpha_0,\theta-\tau\rangle\langle\alpha_0,\theta-\tau|, \quad (8)$$

where we have dropped the subscript RTN for convenience. Thus, at short times, the state consists of two coherent states

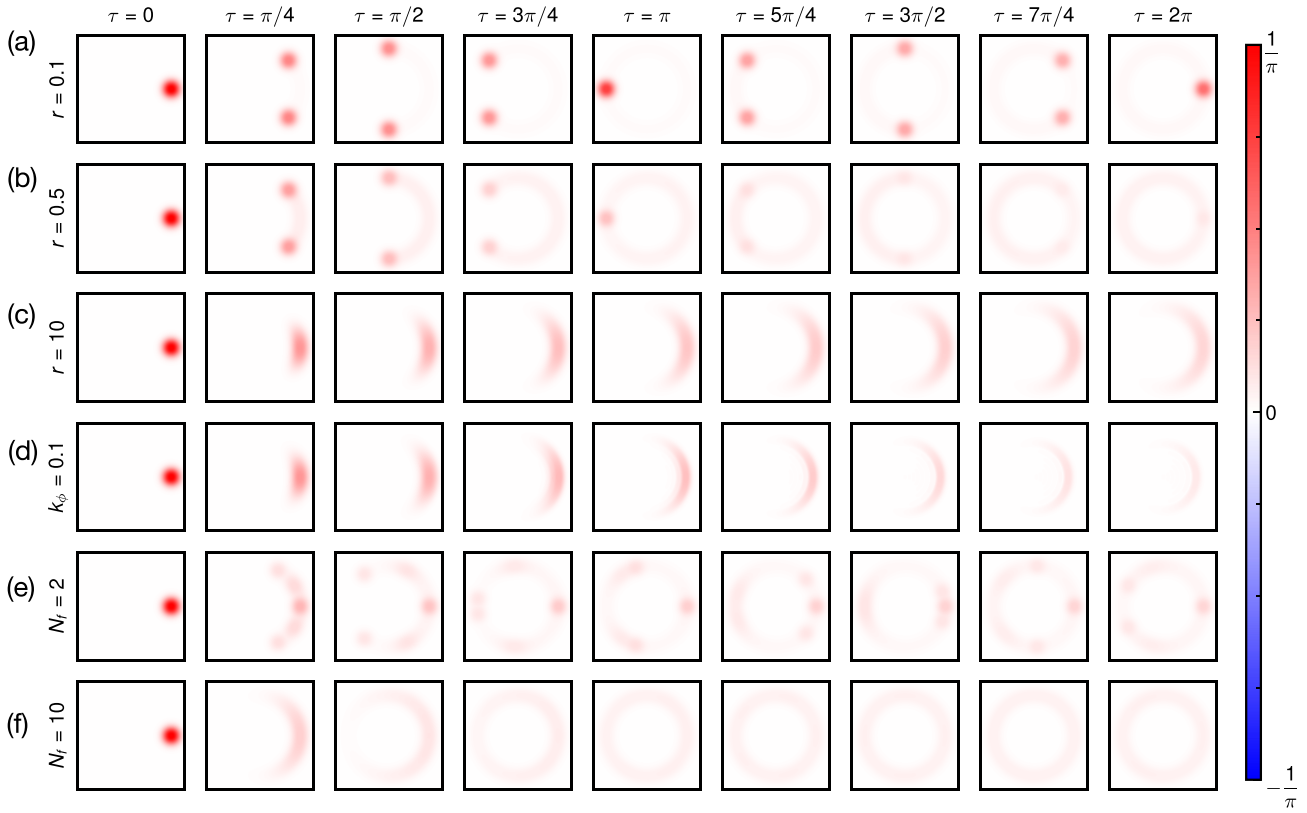

FIG. 1. Evolution of the Wigner function of a coherent state with $\alpha = 2$ under RTN-induced dephasing for (a) $r = 0.1$, (b) 0.5, and (c) 10. For small values of r, the state initially exhibits two distinct lobes, indicative of non-Markovian dynamics, before fully dephasing. As the ratio r increases, the behavior transitions to one resembling Gaussian dephasing [panel (d) where dephasing follows a Gaussian decay rate $k_\phi = 0.1$]. Under $1/f$ noise [panels (e) and (f)], similar non-Markovian "bloblike" features appear in the Wigner function for a small number of fluctuators N_f. When N_f is increased to 10 [panel (f)], the behavior becomes similar to that of the Gaussian case.

with phase angles evolving in opposite directions. This explains the bloblike behavior observed in the phase space, as shown in Fig. 1(a).

In the other limit where $r \gg 1, m, n$, we expand Ω up to $O(1/r)$, and the evolved density matrix in the Fock basis takes the form

$$\hat{\rho}(t) = \sum_{m,n=0}^{\infty} e^{-\frac{1}{2}\frac{(m-n)^2\tau}{r}} \rho_{m,n} |m\rangle\langle n|. \tag{9}$$

For a Gaussian dephasing channel, the evolved density matrix of a state written in Fock basis has the form $\hat{\rho}_G(t) = \sum_{m,n=0}^{\infty} e^{-\frac{1}{2}(m-n)^2\sigma^2} \rho_{m,n} |m\rangle\langle n|$ (see Appendix C). By comparing this with the result above, we find that the RTN dephased state in the large r limit is similar to that of a Gaussian dephasing channel with an effective dephasing rate $k'_\phi = \nu^2/\xi$.

III. QUANTIFYING NON-MARKOVIANITY

Among the different notions of quantum Markovianity specifically devised to deal with continuous variables (CVs) [45,46,62,63], we will focus here on the Breuer-Laine-Piilo (BLP) measure [47,64] based on the trace distance between two states. The trace distance between the states $\hat{\rho}_1$ and $\hat{\rho}_2$ is defined as [47]

$$D(\hat{\rho}_1, \hat{\rho}_2) = \tfrac{1}{2}\mathrm{Tr}|\hat{\rho}_1 - \hat{\rho}_2| = \tfrac{1}{2}\mathrm{Tr}\sqrt{(\hat{\rho}_1 - \hat{\rho}_2)^\dagger(\hat{\rho}_1 - \hat{\rho}_2)}. \tag{10}$$

In addition to being a metric, the trace distance has a clear physical interpretation, as it directly quantifies the distinguishability between two states [47]. The key idea behind this measure is that a Markovian process, which involves continuous information flow from the system to the environment, tends to reduce the distinguishability between any two states over time. In contrast, for non-Markovian processes, which allow for information backflow, the distinguishability between states can increase at certain time intervals. These revivals in the trace distance over time are a signature of non-Markovianity [47,48,65,66]. Given the rate of change of the trace distance,

$$\sigma(t, \hat{\rho}_{1,2}(t)) = \frac{d}{dt} D(\hat{\rho}_1(t), \hat{\rho}_2(t)), \tag{11}$$

Markovian processes are defined by the condition $\sigma(t, \hat{\rho}_{1,2}(t)) \leqslant 0$ for all times t and for all pairs of initial states $\hat{\rho}_1(0)$ and $\hat{\rho}_2(0)$; i.e., the trace distance is a monotonically decreasing function of time. Instead, for a non-Markovian process, this quantity becomes greater than zero for some time intervals, indicating a backflow of information to the system. To quantify this total amount of information flowing from the environment back to the system during the dynamics, the non-Markovianity measure is defined as

$$\mathcal{N}_{\mathrm{BLP}} = \max_{\hat{\rho}_1(0), \hat{\rho}_2(0)} \int_{\sigma>0} dt\, \sigma(t, \hat{\rho}_{1,2}(0)). \tag{12}$$

By construction, the value of this measure $\mathcal{N}_{\mathrm{BLP}}$ is zero for Markovian processes and is greater than zero for non-Markovian processes.

Notably, in Appendix D we have also cross-checked our results with another measure of non-Markovianity related to the Wigner negativity of a state. We see that the two approaches agree qualitatively; hence, we focus on the trace-distance-based measure for the rest of the analysis.

A. $\mathcal{N}_{\mathrm{BLP}}$ for Gaussian states

In this subsection, we characterize the non-Markovianity as measured by BLP for Gaussian states for RTN and for $1/f$ noise. To investigate the non-Markovian effects induced by RTN, we analyze the evolution of the trace distance between two initial bosonic modes, focusing on the occurrence of revivals. The $\mathcal{N}_{\mathrm{BLP}}$ measure is then evaluated by maximizing the summation of revivals over all possible bosonic states. However, this maximization is computationally prohibitive due to the unbounded domain of several parameters involved for the infinite set of CV states. We thus begin by confining our investigation to a broad class of Gaussian states. A general Gaussian state is expressed as [61]

$$\hat{\rho}^{G} = \hat{D}(\alpha)\hat{S}(\beta)\hat{\nu}_{\mathrm{th}}(\tilde{N})\hat{S}^{\dagger}(\beta)\hat{D}^{\dagger}(\alpha), \tag{13}$$

where $\hat{D}(\alpha) = \exp(\alpha\hat{a}^{\dagger} - \alpha^{*}\hat{a})$ is the displacement operator, $\hat{S}(\beta) = \exp(\frac{1}{2}(\beta\hat{a}^{\dagger 2} - \beta^{*}\hat{a}^{2}))$ is the squeezing operator, and $\hat{\nu}_{\mathrm{th}} = \tilde{N}^{\hat{a}^{\dagger}\hat{a}}/(\tilde{N}+1)^{(\hat{a}^{\dagger}\hat{a}+1)}$ is the thermal equilibrium state with $\tilde{N}$ average photon number. The parameters α and β are complex numbers characterized by their amplitude and phase (α_0, θ) and $\alpha = \alpha_0 e^{i\theta}$ and $\beta = \beta_0 e^{i\gamma}$, respectively. The parameter α determines the position of the state in the phase space, and β specifies the magnitude and direction of squeezing. To evaluate $\mathcal{N}_{\mathrm{BLP}}$, the optimization spans ten real parameters from the initial two Gaussian states: $(\alpha_{0_1}, \alpha_{0_2}, \theta_1, \theta_2, \beta_{0_1}, \beta_{0_2}, \gamma_1, \gamma_2, \tilde{N}_1, \tilde{N}_2)$. This procedure is computationally intensive, as the domains of some of the above parameters are unbounded. However, we see that not all ten parameters are relevant to the maximization procedure. We compute the sum of trace-distance revivals for a specific pair of states and define this quantity as $\mathcal{N}^{*}_{\mathrm{BLP}}$ (denoted with an asterisk):

$$\mathcal{N}^{*}_{\mathrm{BLP}}(\hat{\rho}_1(0), \hat{\rho}_2(0)) = \int_{\sigma>0} \mathrm{d}t\ \sigma(t, \hat{\rho}_{1,2}(0)). \tag{14}$$

This quantity is still dependent on the chosen initial states.

As detailed in Appendix E, we begin by optimizing the bounded parameters θ and γ, and we see that we obtain the maximum value of $\mathcal{N}^{*}_{\mathrm{BLP}}$ when $|\theta_1 - \theta_2| = \pi$ and $\gamma_1 = \gamma_2 = 2\theta_1$. All the combinations of θ_1 and θ_2 and values of γ_1 and γ_2 that satisfy the above condition have the same value of $\mathcal{N}^{*}_{\mathrm{BLP}}$ owing to the dephasing nature of the random telegraph noise. Now, we consider the parameters α_0, β_0, and $\tilde{N}$ for a given state, and we see that $\mathcal{N}^{*}_{\mathrm{BLP}}$ is maximized when $\alpha_{0_1} = \alpha_{0_2} = \alpha_0$, $\beta_{0_1} = \beta_{0_2} = \beta_0$, and $\tilde{N}_1 = \tilde{N}_2 = \tilde{N}$. This reduces the optimization to three parameters: α_0, β_0, and $\tilde{N}$. Upon further analysis, we observe in Appendix E that neither the average number of quanta nor the squeezing parameter increases the measure of non-Markovianity. Thus $\mathcal{N}^{*}_{\mathrm{BLP}}$ is maximized for a given value of α_0 with $\beta_0 = 0$ and $\tilde{N} = 0$.

In Fig. 2(a), we plot the evolution of trace distance as a function of τ for $r = 0.1$ for a pair of coherent states with $\alpha_0 = 4$ and phase difference of π, squeezed states with $\beta_0 = 0.4$ and thermal states with $\tilde{N} = 2$ in the non-Markovian regime. While oscillations indicating non-Markovian behavior are present in the cases of squeezed and thermal states, their amplitudes are reduced relative to those of coherent states. This results in the measure of non-Markovianity $\mathcal{N}^{*}_{\mathrm{BLP}}$ being maximum for the coherent states among the three cases. We further illustrate the Wigner evolution of two initial states $\alpha_0 = 4$ and phase difference π. The periodic oscillations in the trace distance can be qualitatively understood from this visualization. When τ equals odd multiples of $\pi/2$, significant overlap between the initial blobs causes $\hat{\rho}_1 - \hat{\rho}_2 \to 0$, resulting in a dip in the trace distance at those times.

Finally, we examine the maximum value of $\mathcal{N}^{*}_{\mathrm{BLP}}$ as a function of α_0 for a fixed r. We find that a specific value of α_0, that we call $\alpha_{0_{\mathrm{max}}}$, maximises the measure, and this value increases with r. The plots $\mathcal{N}^{*}_{\mathrm{BLP}}$ as a function of α_0 for different values of r are given in Fig. 2(b). For the values of r considered, we see from our numerical calculations that for the class of Gaussian states represented by Eq. (13), a pair of coherent states with a particular amplitude $\alpha_{0_{\mathrm{max}}}$ maximizes the non-Markovian measure. Although the analytical relationship between $\mathcal{N}^{*}_{\mathrm{BLP}}$ and $\alpha_{0_{\mathrm{max}}}$ remains elusive, our numerical results indicate that the value of $\alpha_{0_{\mathrm{max}}}$ increases with increase in the value of the ratio r, making it computationally challenging for higher photon numbers. We also observe, as expected, that the value of $\mathcal{N}^{*}_{\mathrm{BLP}}$ increases when r decreases, since this corresponds to going into a stronger non-Markovian regime. In the non-Markovian regime of RTN, the fluctuator does not act as a rapidly varying classical field but instead behaves as a finite-dimensional memory that remains correlated with the bosonic mode over extended times. The system acquires conditional phase shifts depending on the state of the TLS, leading to the build-up of system-environment correlations. When the fluctuator switches state, part of the phase information previously transferred to the environment is returned to the system, resulting in revivals of the trace distance. The latter can be thus seen as information backflow originating from coherent system-TLS dynamics and are suppressed in the fast-switching (Markovian) regime.

Coming to the $1/f$ noise, in Fig. 2(c), we plot the numerical results for the simulation of $1/f$ noise for a pair of coherent states with different values of α. We have fixed the range of values of r, over which the integration to be obtain the evolved density matrix is performed, to be $[10^{-4}, 10^{4}]$. However, we see that values above $r = 1$ do not contribute significantly to the non-Markovianity. The results show that as N_f increases, the oscillation amplitude of the trace distance diminishes [see Fig. 11(a) in Appendix J]. Consequently, the non-Markovianity measure exponentially decreases with increasing N_f. Experimental studies often report a small number of fluctuators coupling to the system of interest [29,32]. Therefore, in realistic scenarios where $N_f \lessapprox 10$, significant non-Markovian behavior is still expected, as reflected in our results.

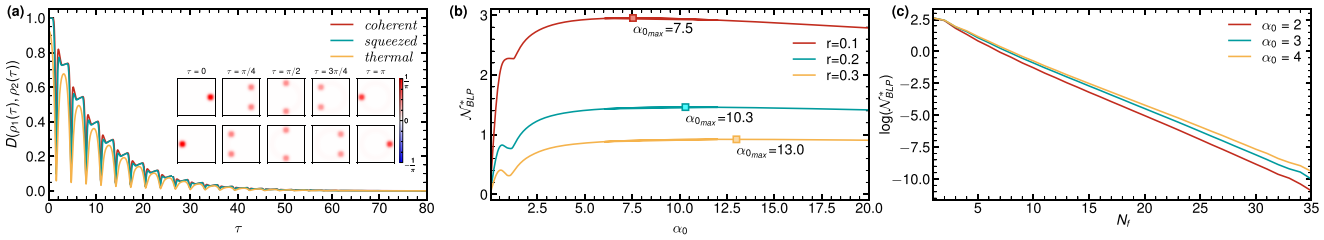

FIG. 2. (a) Evolution of the trace distance between pairs of quantum states: coherent states with $\alpha_1 = -\alpha_2 = 4$ (red), squeezed states with $\beta_1 = \beta_2 = 0.4$ (blue), and thermal states with $\tilde{N}_1 = \tilde{N}_2 = 2$ (yellow). We see that squeezing and thermal fluctuations lead to a suppression of oscillation amplitudes in the trace-distance dynamics, thereby reducing the effective non-Markovianity measure $\mathcal{N}^*_{\mathrm{BLP}}$. (b) For Gaussian states, we show that for a given pair of coherent states with α_0 and $-\alpha_0$, the value of α_0 that maximizes $\mathcal{N}^*_{\mathrm{BLP}}$ depends on r. (c) The behavior of $\mathcal{N}^*_{\mathrm{BLP}}$ as a function of the number of fluctuators N_f in the simulation of $1/f$ noise. For all considered values of $\alpha = 2, 3, 4$ for coherent states, $\mathcal{N}^*_{\mathrm{BLP}}$ decreases exponentially with N_f, indicating a transition toward a Markovian regime.

B. N_{BLP} for non-Gaussian states

While we cannot establish a universal bound on non-Markovianity for all bosonic states, it is instructive to investigate non-Markovian effects within a subclass of non-Gaussian states known as RSB codes [24], which have demonstrated robust error-correcting properties [25,27]. These codes possess discrete rotation symmetry of order N, meaning the code words are $+1$ eigenstates of the operator $\hat{R}_N = e^{i\frac{2\pi}{N}\hat{n}}$. Furthermore, the operator $\hat{Z}_N$, defined as the square root of $\hat{R}_N$, functions as a logical Z operator such that the logical code words $|0\rangle_N$ and $|1\rangle_N$ satisfy

$$\hat{Z}_N|j\rangle_N = (-1)^j|j\rangle_N, \quad \text{for } j \in \{0, 1\}.$$

These code words can be expressed either as rotated superpositions of a primitive state or equivalently expanded in the Fock basis. Detailed constructions of the RSB code words are provided in Appendix F.

In this work, we focus on two specific classes of RSB codes: binomial codes and cat codes. The performance of these codes has been extensively studied in Refs. [25,27], demonstrating promising results for state recovery using error-correction circuits under the effects of photon loss and Gaussian dephasing. Additionally, Refs. [28,67,68] study RSB codes under various other noise models. For cat codes, the primitive state is a coherent state, and the code words are characterized by N, the order of rotation symmetry, and α, the amplitude and phase of the coherent state. In contrast, binomial codes are specified by two parameters, N and K, where K denotes the truncation limit in the Fock basis expansion and determines the maximum order of correctable loss, gain, and dephasing errors (see Appendix F for further details).

The non-Markovian effects on the evolution of the binomial code words in the presence of RTN as a function of the noise strength and covering both Markovian and non-Markovian regimes are provided in Figs. 3(a) and 3(b). We observe that the period of oscillations depends linearly on the order of rotation symmetry N; however, the peaks of the oscillations only broaden with an increase in K. Here, we evaluate the non-Markovian measure $\mathcal{N}^*_{\mathrm{BLP}}$ for the corresponding cases of cat states.

In Fig. 3(a), we see that $\mathcal{N}^*_{\mathrm{BLP}}$ for the case of cat states ($|+\rangle_{2,\alpha}$ and $|-\rangle_{2,\alpha}$) compared to the coherent states ($|+\alpha\rangle$ and $|-\alpha\rangle$) for the same value of α, doubles in magnitude. This directly reflects the doubling of the frequency of the trace distance due to the underlying $N = 2$ symmetry of the code. For similar reasons, we notice in Fig. 3(b) that $\mathcal{N}^*_{\mathrm{BLP}}$ for binomial code linearly increases with the order of symmetry of the code N. As a further remark, we show in Appendix G that for a general state in the span of Fock states $|0\rangle$ and $|l\rangle$ where $l \in \mathbb{N}$, the value of the non-Markovian measure goes to infinity as $l \to \infty$. An analysis of the effects of $1/f$ noise on the code words of the binomial states ($|+\rangle_{1,2}$ and $|-\rangle_{1,2}$) is provided in Fig. 3(c), where we again see that the nonmonotonic behavior in the trace distance dies out as $N_f \gtrsim 10$. This is similar to the case of pair of the coherent states, and thus we also expect an exponential decay of $\mathcal{N}^*_{\mathrm{BLP}}$ as a function of N_f even for the case of binomial codes.

IV. PERFORMANCE OF RSB CODES UNDER RTN DEPHASING AND $1/f$ NOISE

Knill-type teleportation-based error-correction circuits adapted for RSB codes have been numerically analyzed in prior works [25,27]. The results from Ref. [27] for RSB codes find enhanced performance under idealized measurement scenarios, and Ref. [25] extends the work to physically relevant measurement schemes. However, their analysis has predominantly focused on noise models incorporating loss and Gaussian dephasing. Here we extend this investigation to more realistic dephasing environments characterized by random telegraph noise and $1/f$ noise. We assume idealized conditions for state preparation, gate operations, and auxiliary qubits [25,27] to isolate the effects of these dephasing channels. Our analysis focuses on how the code performance evolves with varying RTN parameters, transitioning from the Markovian to non-Markovian regimes.

The Knill EC circuit for RSB codes, as introduced in [27] and shown in Fig. 4, includes the preparation of $|+\rangle_N$ states, CROT gates (controlled rotations) that act as logical controlled-Z gates on logical code words, and measurements to distinguish logical code words in the dual basis. The protocol performs two consecutive one-bit teleportations to transfer the encoded state onto a fresh auxiliary mode, mitigating accumulated noise.

The data rail holds the initial logical state $\hat{\rho}_N = \sum_{i,j=0}^{1} \rho_{ij}|i\rangle_N\langle j|_N$ encoded in an order-N rotation code is subjected to a combined noise channel, with photon loss and RTN

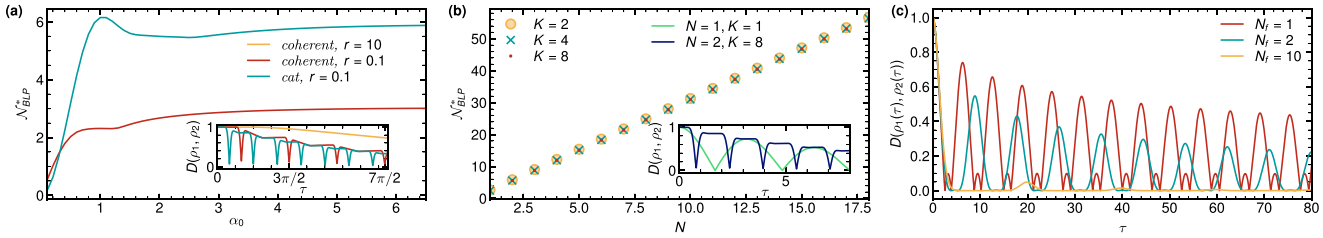

FIG. 3. (a) Non-Markovianity measure $\mathcal{N}^*_{\mathrm{BLP}}$ for $r = 0.1$ as a function of the parameter α_0, evaluated for a pair of coherent states with $\alpha_0 = 2$ and a phase difference of π (shown in red) and the code words of cat states $|+\rangle_{2,\alpha}$ and $|-\rangle_{2,\alpha}$ (shown in blue). The measure is almost twice in the latter case. In the inset, we show that for the cat states, the oscillation period of the trace distance between the code words is half that of a pair of coherent states with the same α, resulting in doubly frequent revivals and a non-Markovianity measure nearly twice that of the coherent states. Additionally, in the inset, we show in yellow how the oscillations in the trace distance disappear in the Markovian limit of $r = 10$. (b) Non-Markovianity measure for binomial code words (non-Gaussian states) as a function of the order of rotation symmetry N. The measure linearly increases with N, due to the linear increase of frequency of oscillations in the trace distance between the code words (shown in the inset). (c) Evolution of the trace distance between pair of binomial states $|+\rangle_{1,2}$ and $|-\rangle_{1,2}$ subjected to $1/f$ noise arising from N_f fluctuators with a distribution of frequency ratios ranging from 10^{-4} to 10^4. We see that the oscillations begin to disappear as the value of N_f increases, suggesting a transition from non-Markovian to Markovian behavior as N_f increases. The non-Markovian measure $\mathcal{N}^*_{\mathrm{BLP}}$ is also consequently expected to go to zero as $N_f \gtrsim 10$.

dephasing. The photon loss channel has the Kraus operators, which are given as $\hat{A}_k = \frac{(1-e^{-\kappa t})^{k/2}}{\sqrt{k!}} e^{-\kappa \hat{n} t/2} \hat{a}^k$ [27], with $\hat{a}$ being the annihilation operator, $\hat{n} = \hat{a}^\dagger \hat{a}$, the number operator, and κ being the loss rate. For RTN dephasing, we numerically obtain Kraus operators from the channel's superoperator formulation [Eq. (2) can be easily recast into superoperator form]. The details of the circuit components, the measurement scheme and the derivation of the final recovery map is provided in Appendix H. We primarily use canonical phase measurements for which $B_{mn} = 1$ [69]. However, we also evaluate the performance under adaptive homodyne detection [70,71], an improved physically implementable measurement scheme.

The postmeasurement recovery map, summed over outcomes x_1, x_2, is given by

$$\mathcal{R} \circ \mathcal{N}(\hat{\rho}_N) = \frac{1}{4} \sum_{x_1, x_2} \hat{P}^\dagger_{i^*(\vec{x})} \left[\sum_{i,j=0}^{3} c_{ij}(\vec{x}) \hat{P}_i \hat{\rho}_L \hat{P}^\dagger_j \right] \hat{P}_{i^*(\vec{x})}, \quad (15)$$

where $\hat{P}_i \in \{\mathbb{I}, X, Z, XZ\}$ are logical Pauli operators on the final order-L code state $\hat{\rho}_L$. The decoder selects the most likely Pauli correction $i^* = \arg\max_i \mathrm{Tr}[\hat{M}_{x_1} \otimes \hat{M}_{x_2} \hat{\mathcal{U}}_c \circ \mathcal{N} \circ \hat{\mathcal{U}}_c^\dagger |i\rangle\langle i|]$ with $\hat{\mathcal{U}}_c = \mathrm{CROT}_{NM} \circ \mathrm{CROT}^\dagger_{NM}$, $\hat{M}$ being the positive operator-valued measure (POVM) for phase measurements and the basis states $|i\rangle = H|a\rangle_N \otimes H|b\rangle_M$.

We compute the average gate fidelity [72] $\mathcal{F}_{\mathrm{EC}}$ of the resulting output state to assess the performance of these codes.

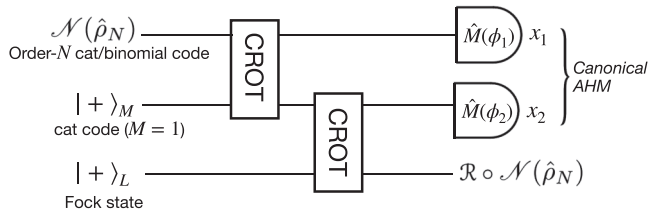

FIG. 4. Teleportation-based Knill EC circuit for bosonic codes.

The average gate fidelity of a quantum channel $\mathcal{E}$ is defined by

$$\mathcal{F}(\mathcal{E}) = \int \mathrm{d}\psi \ \langle\psi|\mathcal{E}(|\psi\rangle\langle\psi|)|\psi\rangle, \quad (16)$$

where $\mathrm{d}\psi$ is a uniform measure on the state space, normalized to unity: $\int \mathrm{d}\psi = 1$.

A. Numerical results: Non-Markovian effects in the error-correcting performance of binomial codes

In this subsection, we present the numerical results of the performance of the error-correction protocol, obtained by calculating the average gate fidelity [72], $\mathcal{F}_{\mathrm{EC}}$ of the output quantum channel obtained after applying the most likely Pauli correction. We further analyze this as a function of various parameters of the noise model and the input encoding state.

In Fig. 5, we present the infidelity $(1 - \mathcal{F}_{\mathrm{EC}})$ as a function of τ corresponding to binomial code words subjected to RTN dephasing with $r = 0.1$ and a photon loss channel with

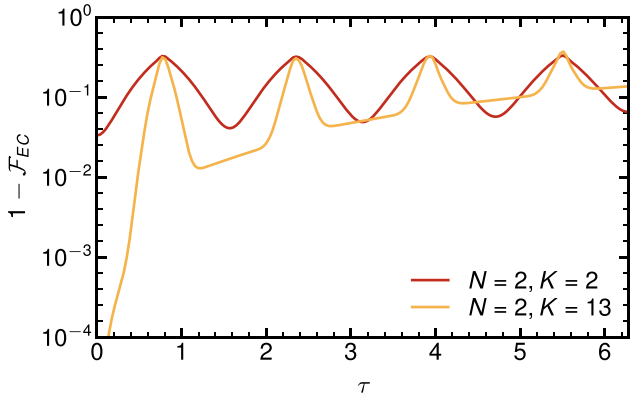

FIG. 5. Infidelity from the Knill EC circuit for a binomial code with the given parameters in the non-Markovian limit of $r = 0.1$ with a loss channel of strenght $\kappa/\nu = 0.01$. We notice that the frequency of oscillations depends only on the order of symmetry N. For higher values of K, we see that the width of the oscillations increases, resulting in longer time intervals with increased performance.

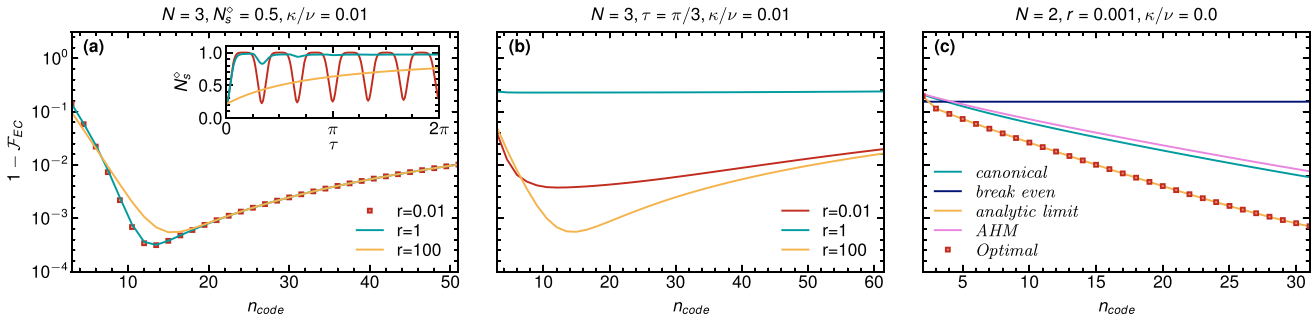

FIG. 6. (a) Infidelity of the error-corrected state recovered using the Knill EC circuit, shown for various values of the parameter r, ranging from the Markovian regime ($r = 100$) to the non-Markovian regime ($r = 0.01$), in the presence of an additional photon loss channel with $\kappa/\nu = 0.01$ as a function of average photon number of the binomial code. The noise strength of different r and for each value of K has been fixed to be $N_s^\diamond = 0.5$. The inset shows the oscillatory behavior of the noise strength with τ for $K = 8$ (which has the least infidelity for $N = 3$). We see that the codes perform significantly well and are qualitatively similar for all values of r at a given noise strength. However, in panel (b), for a fixed $\tau = \pi/3$, since the noise strength is the highest for $r = 1$, the code performs worse for this case. The performance is therefore sensitive to τ for a given r. In the non-Markovian regime, we can expect good performance even at larger but specific values of τ due to the oscillatory feature of the noise. From the inset of panel (a), we can see that there are periodically occurring times for which the noise strength becomes small, leading to better performance for those values of τ. (c) Infidelity under pure RTN dephasing (no loss) in the strongly non-Markovian regime ($r = 0.001$) for $N = 2$ and $\tau = 1$. The performance of the Knill EC circuit (with canonical phase measurements) is compared with the analytically computed fidelity limit, the breakeven threshold, optimal recovery map, by using adaptive homodyne detection measurements.

$\kappa/\nu = 0.01$ for encoding parameters: $N = 2, K = 2$ (red) and $N = 2, K = 13$ (yellow). We observe that there are oscillations with τ in the non-Markovian regime with the frequency of these oscillations depending on N and the width of the dips depending on K. To understand this better, we derive a semianalytical expression for the average gate fidelity under a general dephasing channel (see Appendix I). Assuming canonical phase measurements [Eq. (H3)], the fidelity takes the form

$$\mathcal{F} = \frac{1}{2} + \frac{1}{12}\Bigg[\int_0^{2\pi} d\phi_1 \left|c_0^N - c_1^N\right|(\phi_1) + \int_0^{2\pi} d\phi_2 \left|c_0^M - c_1^M\right|(\phi_2)\Bigg] + \frac{1}{24}\int_0^{2\pi} d\phi_1 \left|c_0^N - c_1^N\right|(\phi_1)\int_0^{2\pi} d\phi_2 \left|c_0^M - c_1^M\right|(\phi_2),$$

where

$$c_{0/1}^N(\phi_1) = \mathrm{Tr}[\hat{M}(\phi_1)\mathcal{N}(|\pm\rangle\langle\pm|_N)],$$

$$c_{0/1}^M(\phi_2) = \mathrm{Tr}[\hat{M}(\phi_2)|\pm\rangle\langle\pm|_M],$$

where the auxiliary qubit is assumed to be noiseless.

For $K = 2$ and arbitrary N, we find (see Appendix I for derivation)

$$\int_0^{2\pi} d\phi_1 \left|c_0^N - c_1^N\right|(\phi_1) = \frac{4\sqrt{2}}{\pi}|G(N, r, \tau)|,$$

which is proportional to the modulus of the dephasing function $|G(r, \tau)|$ in Eq. (3), oscillating with frequency $\Omega = 2\sqrt{N^2 - r^2}$. For small r, Ω becomes nearly linear in N. Fixing N and increasing K gives a contribution to the fidelity from frequencies higher than Ω, resulting in broader dips in infidelity, and increasingly favorable time windows for correction. These trends agree with the numerical simulations presented in Fig. 5, where we see that in the non-Markovian regime, while keeping N and κ/ν fixed, increasing K modifies the width of the fidelity dips, thus increasing our chances of remaining in the time intervals of better performance. However, larger values of K also enhance the impact of photon loss, necessitating a careful optimization of K for fixed system parameters.

In Figs. 6(a) and 6(b), we plot the infidelity $(1 - \mathcal{F}_{\mathrm{EC}})$ as a function of the average photon number of the code n_{code} for a fixed loss rate $\kappa_\phi = 0.01$, various values of r and for (a) fixed noise strength $N_s^\diamond$ and various values of τ, and (b) fixed value of τ and various values of $N_s^\diamond$. The average photon number is calculated as

$$n_{\mathrm{code}} = \tfrac{1}{2}\mathrm{Tr}[(|0\rangle\langle 0|_N + |1\rangle\langle 1|_N)\hat{n}],$$

and for binomial codes, we have $n_{\mathrm{code}} = \frac{1}{2}NK$. We characterize the noise strength in a channel by evaluating the diamond norm of the channel after being projected to the codespace. Defining the projector operator that takes a state from Fock basis $\{|0\rangle, |1\rangle\}$ to the codespace of an RSB code spanned by $\{|0\rangle_N, |1\rangle_N\}$ where N is the order of rotation symmetry of the code, we have

$$\hat{S} = |0\rangle_L\langle 0| + |1\rangle_L\langle 1|. \tag{17}$$

The superoperator form $\mathcal{E}$ of the noise channel map that arises for loss, RTN, or $1/f$ dephasing can then be projected onto the codespace as

$$\mathcal{E}' = \hat{\hat{S}}^\dagger \mathcal{E}\hat{\hat{S}}, \tag{18}$$

where $\hat{\hat{S}}$ is the superoperator form of $\hat{S}$. We then evaluate the diamond norm $||\mathcal{E}'||^\diamond$ [73–75] of this channel numerically and define noise strength as

$$N_s^\diamond = 1 - ||\mathcal{E}'||^\diamond. \tag{19}$$

The identity channel will give $||\mathcal{E}'||^{\diamond} = 1$. The inset of Fig. 6(a) shows the behavior of the noise strength as a function of τ. We see that due to the non-Markovian nature of the noise, for $r = 0.01$, we have oscillations in the noise that fade away as we increase r.

In Fig. 6(a), we see that for $N_s^{\diamond} = 0.5$, the binomial code with $N = 3$ for a loss rate of $\kappa/\nu = 0.01$ performs reasonably well for all values of r for Markovian to non-Markovian limits. In Fig. 6(b), if we instead fix the value of τ, we notice that $r = 1$ yields a poor performance. This also corresponds to the noisiest state for a given τ in the inset of Fig. 6(a), consequently leading to lower values of fidelity. Thus, the performance of these codes for a given r depends on N and τ.

In Fig. 6(c), we consider infidelity versus n_{code} for $r = 0.001$ and zero loss, isolating the effect of dephasing at a fixed $\tau = 1$. Since canonical phase measurements, although ideal, are unphysical, a more practical approach for information about the phase distribution is provided by heterodyne detection for which the matrix elements of B are not equal to one for $m \neq n$. An approximate scheme to implement the matrix B in Eq. (H3) is the adaptive homodyne measurement (AHM), which relies on continuously adjusting the local oscillator phase θ based on measurement history [70], to reduce the information gain about photon distribution. We evaluate the performance for AHM and as shown in Fig. 6(c), the performance with AHM closely matches the ideal canonical case to a very good extent. We further compare these results with the performance of an optimal recovery map, obtained via a semidefinite program maximizing fidelity [27,68]. An analytical upper bound on the average gate fidelity can be derived using a well-known inequality relating measurement outcomes to trace distance [76]:

$$\frac{1}{2}\sum_m |p_m - q_m| \leqslant D(\hat{\rho}, \hat{\sigma}),$$

where $p_m = \text{Tr}(\hat{E}_m\hat{\rho})$ and $q_m = \text{Tr}(\hat{E}_m\hat{\sigma})$ are POVM probabilities, and $D(\cdot,\cdot)$ denotes trace distance between the states.

Our case with $\hat{\rho} = \mathcal{N}(|+\rangle\langle+|)$ and $\hat{\sigma} = \mathcal{N}(|-\rangle\langle-|)$ yields the bound

$$\mathcal{F}(\tau) \leqslant \frac{2 + [1 + D(|+_\tau\rangle_N, |-_\tau\rangle_N)][1 + D(|+\rangle_M, |-\rangle_M)]}{6}, \tag{20}$$

where $|\pm_\tau\rangle_N$ are the evolved code words at time τ after being subjected to the dephasing channel (we refer to Appendix I for derivation). This equation shows that the fidelity is limited by the oscillatory behavior of the trace distance between the code words, which also is key to evaluating the non-Markovian measure using BLP. The fidelity limit is plotted in Fig. 6(c) where we observe that it closely follows the results of the optimal recovery map.

To summarize, our results show that recovery fidelity under RTN dephasing depends sensitively on the order of symmetry N and on the time at which the error correction is applied τ. We observe oscillations in $\mathcal{F}_{\text{EC}}$ due to non-Markovian effects, with optimal performance in highly non-Markovian regime ($r \leqslant 10^{-3}$) for certain timescales. We provide an understanding of these oscillations through an analytic expression derived for a purely dephasing channel. In the highly Markovian limit ($r \geqslant 10^2$), RSB codes continue to perform very well for a range of values of the average photon number, reproducing the results of a Gaussian dephasing channel used in [25,27]. For a given τ, in the intermediate regime ($r \sim 1$), the average gate fidelity dips below the breakeven threshold. These findings are highly relevant, as experimental systems such as superconducting qubits and three-dimensional (3D) cavities exhibit RTN parameters in the $r \sim 10^{-4}$ to 10^{-1} range [29,34]. For $1/f$ noise, we find that the codes perform comparably to Gaussian models when the number of fluctuators is $N_f \gtrsim 10$. However, the performance for small N_f shows oscillations as a function of τ (see Appendix J for numerical plots). This work studies the impact of RTN dephasing on non-Gaussian states relevant to QEC.

B. Numerical results: Summarized comparison of different noise channels

We finally compile the results obtained for all channels using the binomial encoding and present them as a function of the noise strength. This allows a direct comparison of how different noise models behave with respect to a common parameter. Figure 7(a) shows the average gate fidelity from the Knill EC circuit with canonical measurements as a function of $N_s^{\diamond}$ for the ($N = 3$, $K = 8$) binomial code under several dephasing channels: RTN with a range of switching rates r spanning non-Markovian (orange dots) to Markovian regimes (blue lines), a Gaussian dephasing channel (pink), and $1/f$ noise generated from ten fluctuators (dark purple). For reference, we also include the performance of a trivial qubit encoding, implemented by mapping logical states to the Fock states $|0\rangle$ and $|1\rangle$, to illustrate the improvement obtained from bosonic encoding. A corresponding analysis for the cat code ($N = 2$, $\alpha^2 = 12$) is presented in Appendix K. As seen in Fig. 7(a), the RSB encoding yields a substantial fidelity enhancement across all noise strengths as compared to the qubit encoding. In the non-Markovian RTN regime, the fidelity varies nonmonotonically with $N_s^{\diamond}$, giving rise to the scattered orange points. For $r > 1$, the fidelity curves become qualitatively similar to—and for large r, nearly indistinguishable from—those of the Gaussian dephasing channel. The $1/f$ noise with ten fluctuators exhibits a similar trend, consistent with its increasingly Markovian behavior in this regime.

To further investigate the dependence on r, we plot the logarithm of the infidelity at fixed noise strengths $N_s^{\diamond} = 0.1$ and $N_s^{\diamond} = 0.4$, corresponding to vertical cuts along the gray dotted lines in Fig. 7. At low noise strength [Fig. 7(b)], the performance does not vary between the non-Markovian and Markovian limits. The inset of Fig. 6(a) confirms that the times at which $N_s^{\diamond} = 0.1$ is reached are nearly identical for $r = 0.01$, 1, and 100. At higher noise strength, e.g., $N_s^{\diamond} = 0.4$, the times remain comparable for $r \leqslant 1$, but in the Markovian limit the state experiences the noise for a longer duration. This provides an intuitive explanation for the reduced fidelities observed for $r > 1$ at larger noise strengths [Fig. 7(c)] for which $N_s^{\diamond} = 0.4$. The same qualitative behavior is found for other binomial encodings and for cat codes as shown in Appendix K.

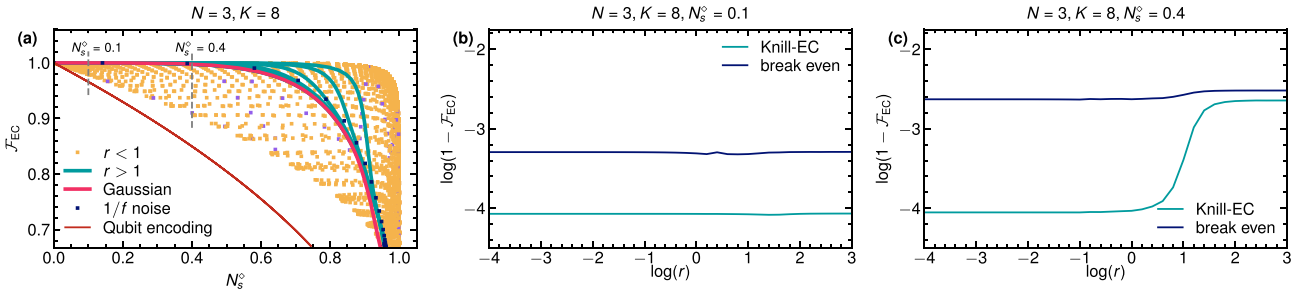

FIG. 7. Average gate fidelity $\mathcal{F}_{\mathrm{EC}}$ of the error-corrected output state from the Knill EC circuit as a function of the noise strength in the input state, induced by dephasing from RTN or $1/f$ noise, for binomial encoding with parameters $N = 3, K = 8$. The orange squares represent the non-Markovian regime with ratio $r < 1$. The fidelity $\mathcal{F}_{\mathrm{EC}}$ for this case exhibits nonmonotonic behavior with respect to the noise strength due to the oscillatory nature of the dephasing function, that is, we plot in purple squares for one such value of $r = 0.1$ in the non-Markovian regime in panel (a). In contrast, for $r > 1$, a monotonic decrease in $\mathcal{F}_{\mathrm{EC}}$ is observed as noise strength increases. The $1/f$ noise, modeled using ten fluctuators with switching rates taken from a distribution, exhibits behavior similar to that of the Gaussian case. Infidelity of the recovered state as a function of r along a fixed line [shown in dotted gray in the plots in panel (a)] is given below for (b) $N_s^{\diamond} = 0.1$ and (c) $N_s^{\diamond} = 0.4$. These results are compared with the breakeven threshold, and we observe that the codes perform better than breakeven for all values of r.

V. DISCUSSION AND CONCLUSIONS

In this work, we investigated the RTN and $1/f$ noise on bosonic modes, where such noise arises from the interaction with one or more TLSs. This class of noise is especially relevant in contemporary quantum hardware platforms such as 3D cavities and superconducting resonators, where strong coupling between TLS and bosonic modes has been experimentally observed [34]. The $1/f$ noise, prevalent across quantum devices, is modeled via either a single RTN fluctuator with distributed switching rates or a set of multiple independent fluctuators coupled to the system.

From an open quantum systems perspective, we characterized the non-Markovian nature of the induced dynamics using the BLP trace-distance-based measure $\mathcal{N}_{\mathrm{BLP}}$. We observed a crossover in dynamics from non-Markovian to Markovian behavior close to $r = 1$, where $r = \xi/\nu$ is the ratio of the RTN switching rate to the coupling strength of the fluctuator to the bosonic mode. In the non-Markovian regime ($r \ll 1$), CV states exhibit revivals in the evolution of trace distance due to information backflow. We showed numerically that, for Gaussian states, the non-Markovianity measure is maximized by specific pairs of coherent states with amplitude depending on the ratio r. Meanwhile, for non-Gaussian states, particularly those used in RSB codes, $\mathcal{N}_{\mathrm{BLP}}$ can grow unboundedly with the code's symmetry order N. In contrast, the Markovian regime ($r \gg 1$) and the effective Markovian limit induced by $1/f$ noise with many fluctuators ($N_f \gtrsim 10$) result in a monotonic degradation of trace distance with time, corresponding to the non-Markovian measure being equal to zero.

We then analyzed the performance of RSB codes—specifically binomial and cat codes—under RTN and $1/f$ noise in addition to a loss channel using a Knill-type teleportation-based QEC circuit. Our results show that encoding with $N > 1$ consistently outperforms the trivial qubit encoding (which also corresponds to $N = 1, K = 1$ for the binomial codes) in both Markovian and non-Markovian regimes. However, in the non-Markovian limit, the average gate fidelity, which is a metric of performance, exhibits periodic oscillations in time, making QEC especially effective at specific time intervals. The frequency of these oscillations increases linearly with N, while their temporal width can be broadened by tuning the code parameters K (binomial) and α (cat). These features allow fidelities to exceed the breakeven threshold significantly, provided error correction is applied in synchrony with these peaks.

In the Markovian regime ($r \gg 1$), as well as under $1/f$ noise with a sufficient number of fluctuators ($N_f \gtrsim 10$), the fidelity degrades monotonically with time. As a function of the average photon number of the code, we still obtain high fidelities above the breakeven threshold, recovering the results of Gaussian dephasing [25]. We further validate the robustness of our findings by comparing the ideal canonical phase measurement with the more experimentally feasible adaptive homodyne detection, observing negligible differences in performance.

Finally, we derived a semianalytical bound on the QEC fidelity for a general purely dephasing channel and found that this bound is governed by the trace distance between code words of the input encoding. In the non-Markovian limit, we are fundamentally limited by the oscillatory behavior in the fidelity. This result bridges our open-system analysis of non-Markovianity in bosonic systems with the results of quantum error correction, highlighting the interplay between noise structure, code symmetry, and error-correction capability.

Our findings provide understanding of how CV codes interact with RTN and $1/f$ noise, and how dynamical memory effects induced by such environments can be exploited to enhance QEC performance in near-term quantum devices. An important direction for future investigation is the extension of the present analysis to noise models that explicitly capture temporal correlations across multiple error-correction cycles. While here we focused on single-cycle effective channels exhibiting information backflow and other dynamical memory effects, a full circuit-level description of non-Markovian noise requires multitime formalisms, such as quantum combs and memory quantum channels [77,78]. These framework account for the different facets of non-Markovianity and provide promising strategies to fully characterize the robustness of bosonic error-correcting codes against general

non-Markovian noise. Other directions for future exploration include gaining a deeper understanding of the behavior observed in the numerical results shown in Fig. 2(b), with the aim of developing better physical intuition for the impact of RTN noise. In the context of error correction, it would also be worthwhile to investigate alternative decoding strategies, potentially replacing the maximum-likelihood estimator with decoders that are better tailored to this specific noise model. Such approaches may further improve performance and provide additional insight into how structured non-Markovian noise can be effectively mitigated.

ACKNOWLEDGMENTS

We acknowledge useful discussions with A. Jayaraman, A. Eriksson, C. Vuillot, D. Sen, K. Helambe, K. Luoma, N. Didier, S. Gasparinetti, and M. Hennrich. We warmly thank S. Maniscalco for helping in the stage of conception of this project. G.F. acknowledges funding from the European Union's Horizon Europe Framework Programme (EIC Pathfinder Challenge project Veriqub) under Grant Agreement No. 101114899. G.F. acknowledges financial support from the Swedish Research Council through the project grant VR DAIQUIRI. G.F., T.H., and A.U. acknowledge support from the Knut and Alice Wallenberg Foundation through the Wallenberg Center for Quantum Technology (WACQT). G.F., A.U., and R.G.A. acknowledge funding from Chalmers Area of Advance Nano. A.S. acknowledges support from MUR under the PON Ricerca e Innovazione 2014–2020 project EEQU and under the PRIN 2022 project "Quantum Reservoir Computing (QuReCo)" (2022FEXLYB).

A.U. performed most of the analytical and numerical calculations and wrote the largest part of the manuscript. T.H. contributed significant insights that helped guide the research direction and provided valuable support in structuring and editing the manuscript. R.G.A. performed analytical and numerical calculations. A.S. provided insights on open quantum systems and to the manuscript. G.F. conceived and supervised the project and wrote parts of the manuscript.

DATA AVAILABILITY

The data that support the findings of this article are not publicly available upon publication because it is not technically feasible and/or the cost of preparing, depositing, and hosting the data would be prohibitive within the terms of this research project. The data are available from the authors upon reasonable request.

APPENDIX A: DERIVATION OF DEPHASING FUNCTION OF RTN

The Hamiltonian for the bosonic mode coupled to the TLS is given by Eq. (1), which we rewrite here: $\hat{H}_{\rm RTN} = \epsilon \hat{a}^\dagger \hat{a} + \nu c(t) \hat{a}^\dagger \hat{a}$. Defining two dimensionless quantities $\tau = \nu t$ and $r = \xi/\nu$, we can express the evolution operator in the interaction picture as

$$\hat{U}(t) = e^{i\phi_{\rm RTN}(\tau)\hat{a}^\dagger \hat{a}}, \tag{A1}$$

where the RTN phase $\phi_{\rm RTN}(\tau)$ is defined as

$$\phi_{\rm RTN}(\tau) = \int_0^\tau c(\tau')d\tau'. \tag{A2}$$

The evolved density matrix is obtained by averaging the evolved density operator over the RTN phase [Eq. (A2)],

$$\hat{\rho}(\tau) = \langle \hat{U}(\tau)\hat{\rho}_0 \hat{U}^\dagger(\tau)\rangle_{\phi_{\rm RTN}(\tau)}. \tag{A3}$$

Next, we consider the initial state $\hat{\rho}_0$ of the bosonic mode expressed in the Fock basis

$$\hat{\rho}_0 = \sum_{m,n=0}^{\infty} \rho_{m,n} |m\rangle\langle n|, \tag{A4}$$

where $\rho_{m,n}$ is the (m, n)th matrix element of the density matrix. The evolved density matrix can thus be written as

$$\hat{\rho}_{\rm RTN}(\tau) = \sum_{m,n=0}^{\infty} \langle e^{i\phi_{\rm RTN}(\tau)(m-n)}\rangle_{\phi_{\rm RTN}(\tau)} \rho_{m,n} |m\rangle\langle n|. \tag{A5}$$

The averaging $\langle\cdots\rangle_{\phi_{\rm RTN}(t)}$ is performed over different instances of the random telegraph stochastic noise. The quantity $\langle e^{i\phi_{\rm RTN}(\tau)(m-n)}\rangle_{\phi_{\rm RTN}(t)}$ is called the dephasing function $G(r, \tau)$, and an analytical expression for it can be derived in two ways. We now briefly derive it in both ways in this Appendix. The first method of derivation involves expanding the functional $G(r, \tau) = \langle e^{i(m-n)\phi(\tau)}\rangle_{\phi(\tau)}$ in time-ordered Taylor series, as [79]

$$G(\tau) = \sum_{k=0}^{\infty} (i(m-n))^k I_k(\tau), \tag{A6}$$

where

$$I_k(\tau) = \int_0^\tau d\tau_1 \int_0^{\tau_1} d\tau_2 \cdots \int_0^{\tau_k} d\tau_k \langle c(\tau_1)c(\tau_2)\cdots c(\tau_k)\rangle. \tag{A7}$$

Using the following relations from the statistics of the noise, $\langle c(\tau_1)c(\tau_2)\rangle = e^{-2r|\tau_1-\tau_2|}$ and $\langle c(\tau_1)c(\tau_2)\cdots c(\tau_n)\rangle = \langle c(\tau_1)c(\tau_2)\rangle\langle c(\tau_3)\cdots c(\tau_n)\rangle$, we differentiate Eq. (A6) twice to obtain a second-order differential equation for $G(\tau)$. The characteristic equation with $G(\tau) = e^{x\tau}$ gives $x^2 + 2rx + (m-n)^2 = 0$ with the two solutions being $x_\pm = -r \pm \sqrt{r^2 - (m-n)^2}$ where r is the ratio fo the switching rate of RTN ξ to the coupling strength ν. The initial conditions $G(0) = 1$ and $G'(0) = 0$ lead to the following solution:

$$G(\tau) = e^{-r\tau}\left(\cosh(\Omega\tau) + \frac{r}{\Omega}\sinh(\Omega\tau)\right), \tag{A8}$$

where $\Omega = \sqrt{r^2 - (m-n)^2}$. Alternatively, we can also derive the probability distribution for $\phi(\tau)$ by following the method used in Ref. [40]. Let $p(\phi, \tau) = p_r(\phi, \tau) + p_l(\phi, \tau)$, where $p_r(\phi, \tau)$, $p_l(\phi, \tau)$ are the probability densities that $c(\tau - \delta\tau) = \pm 1$, respectively, while $\phi(\tau) := \int_0^\tau ds\, c(s) = \phi$ and $\delta\tau$ is taken to be sufficiently small that only one flip can take place at most during $\delta\tau$. It is easy to see that

$$\begin{aligned} &p_r(\phi, \tau + \delta\tau) \\ &\quad = (1 - r\delta\tau)p_r(\phi - \delta\tau, \tau) + r\delta\tau\ p_l(\phi - \delta\tau, \tau), \\ &p_l(\phi, \tau + \delta\tau) \\ &\quad = (1 - r\delta\tau)p_l(\phi + \delta\tau, \tau) + r\delta\tau\ p_r(\phi + \delta\tau, \tau). \end{aligned}$$

Expanding the functions p_r and p_l as a Taylor series of either of its arguments around ϕ and τ, respectively, and taking the limit $\delta\tau \to 0$, we get two coupled differential equations for $p = p_r + p_l$ and $q := p_r - p_l$. Eliminating q, one can find the *telegraph equation*

$$p_{\tau\tau} + 2r p_\tau = p_{\phi\phi}. \tag{A9}$$

A solution to this equation can be found, subject to the initial conditions $p(\phi, 0) = \delta(\phi)$ and $p_\tau(\phi, 0) = 0$ [where the second condition follows from the fact that $P(c(0) = \pm 1) = 0.5$]: $p(\phi, \tau) = \int \frac{dk}{2\pi}(a_k^+ e^{-i\omega_k^+ \tau} + a_k^- e^{-i\omega_k^- \tau})e^{ik\phi}$, $\omega_k^\pm = -ir \pm \sqrt{k^2 - r^2}$, $a_k^\pm = \frac{1}{2}(1 \pm \frac{ir}{\sqrt{k^2 - r^2}})$.

The dephasing factor due to RTN can be directly calculated as follows:

$$\begin{aligned} G(m, n, \tau) &= \int_{-\infty}^{\infty} p(\phi, \tau) e^{i(m-n)\phi} \\ &= a_k^+ e^{-i\omega_k^+ \tau} + a_k^- e^{-i\omega_k^- \tau}|_{k=n-m} \\ &= e^{-r\tau}\Big(\cosh(\Omega\tau) + \frac{r}{\Omega}\sinh(\Omega\tau)\Big), \end{aligned} \tag{A10}$$

in agreement with Eq. (A8).

APPENDIX B: DERIVATION OF THE DENSITY MATRIX UNDER THE INFLUENCE OF MULTIPLE FLUCTUATORS

The widely adopted model for describing $1/f$ noise involves a distribution of switching rates of single RTN fluctuators. For an individual RTN fluctuator, the power spectral density is Lorentzian and is expressed as [41]

$$S_\xi(\omega) = \frac{1}{\pi}\frac{2\nu^2\xi}{\omega^2 + (2\xi)^2}. \tag{B1}$$

The $1/f$ noise behavior can arise from either a single RTN fluctuator with a switching rate drawn from a statistical distribution $P(\xi)$ or a collection of RTN fluctuators with fixed but distinct switching rates, also distributed according to $P(\xi)$. In both cases, the combined spectral density over a frequency range from $\xi_{\min}$ to $\xi_{\max}$ is given by

$$S(\omega) = \int_{\xi_{\min}}^{\xi_{\max}} d\xi P(\xi) S_\xi(\omega). \tag{B2}$$

If the switching rates have a distribution that is proportional to the inverse of the rate, that is, $P(\xi) \propto 1/\xi$ within this range, Eq. (B2) yields $S(\omega) \propto 1/\omega$, consistent with the $1/f$ noise spectrum [41].

We consider a bosonic mode coupled to a fixed number of RTN fluctuators N_f, each with a switching rate sampled from the probability distribution

$$P(\xi) = \frac{1}{\ln\left(\frac{\xi_{\max}}{\xi_{\min}}\right)}\frac{1}{\xi}. \tag{B3}$$

We assume a uniform coupling strength for all fluctuators, with the switching rates following the above distribution $P(\xi)$. The Hamiltonian as written in Eq. (4) is given by $\hat{H}_{1/f} = \epsilon\hat{a}^\dagger\hat{a} + \frac{\nu}{\sqrt{N_f}}\sum_{i=1}^{N_f} c_i(t)\hat{a}^\dagger\hat{a}$, where the ith fluctuator has a switching rate ξ_i. With a similar change of variables $\tau = \nu t$ and $r = \xi/\nu$, for a general bosonic state, the evolved density matrix can be written as

$$\hat{\rho}_{1/f}(\tau) = \sum_{m,n=0}^{\infty} \langle e^{i\Phi_{1/f}(\tau)(m-n)}\rangle_{\Phi_{1/f}(\tau)} \rho_{m,n}|m\rangle\langle n|. \tag{B4}$$

Here, $\Phi_{1/f}(\tau) = \frac{1}{\sqrt{N_f}}\sum_i \phi_{i,\mathrm{RTN}}(\tau)$, where $\phi_{i,\mathrm{RTN}}(\tau) = \int_0^\tau d\tau' c_i(\tau')$. The averaging operation $\langle\cdot\rangle_{\Phi_{1/f}(\tau)}$ can be computed explicitly as follows:

$$\begin{aligned} &\langle e^{i\sum_i \phi_{i,\mathrm{RTN}}(\tau)(m-n)}\rangle_{\Phi_{1/f}(\tau)} \\ &\quad = \langle e^{i\phi_{1,\mathrm{RTN}}(\tau)(m-n)} e^{i\phi_{2,\mathrm{RTN}}(\tau)(m-n)} \cdots\rangle \\ &\quad = (\overline{\langle e^{i\phi_{\mathrm{RTN}}(\tau)(m-n)}\rangle})^{N_f}, \end{aligned} \tag{B5}$$

where the first averaging $\langle\cdots\rangle_{\phi_{\mathrm{RTN}}(t)}$ is over different instances of the RTN as before, the second averaging operation $\overline{\langle\cdots\rangle}$ is performed over the distribution of switching rates of the fluctuators, and $\phi_{\mathrm{RTN}}(\tau)$ is a function of the ratio r. Using the distribution $P(r)$, the dephasing function is expressed as

$$\langle e^{i\sum_i \phi_{i,\mathrm{RTN}}(\tau)(m-n)}\rangle = \left(\int_{r_{\min}}^{r_{\max}} dr\ \langle e^{i\phi_{\mathrm{RTN}}(\tau)(m-n)}(r)\rangle P(r)\right)^{N_f}, \tag{B6}$$

where $r_{\min}$ and $r_{\max}$ are the minimum and maximum values of the ratio of switching rate to coupling strength that a single or multiple TLSs can have. Substituting the previously derived expression for the dephasing function Eq. (3), this integral can be evaluated analytically as shown below. Substituting $P(r) = 1/r$, the integral becomes

$$\int_{r_{\min}}^{r_{\max}} \frac{dr}{r} e^{-r\tau}\Big(\cosh\Omega\tau + \frac{r}{\Omega}\sinh\Omega\tau\Big), \tag{B7}$$

where $\Omega = \sqrt{r^2 - a^2}$ for $a = (m - n)$. Writing $r_{\min} = r_{\mathrm{m}}$ and $r_{\max} = r_{\mathrm{M}}$ for convenience, and assuming $r_{\mathrm{m}} < a < r_{\mathrm{M}}$, we split this integral into two parts, with $I = I_1 + I_2$.

$$I_1 \equiv \int_{r_{\mathrm{m}}}^{a} \frac{dr}{r} e^{-r\tau}\Big(\cos\Omega'\tau + \frac{r}{\Omega'}\sin\Omega'\tau\Big), \tag{B8}$$

$$I_2 \equiv \int_{a}^{r_{\mathrm{M}}} \frac{dr}{r} e^{-r\tau}\Big(\cosh\Omega\tau + \frac{r}{\Omega}\sinh\Omega\tau\Big), \tag{B9}$$

where in I_1, $\Omega' = \sqrt{a^2 - r^2}$. Performing the integral for the three cases, we obtain

$$I = \begin{cases} F(z_M^+) + F(z_M^-) - F(z_m) - F(z_m^*), & r_{\mathrm{m}} < a < r_{\mathrm{M}}, \\ F(z_M^+) + F(z_M^-) - F(z_m^+) - F(z_m^-), & a < r_{\mathrm{m}} < r_{\mathrm{M}}, \\ F(z_M) + F(z_M^*) - F(z_m) - F(z_m^*), & r_{\mathrm{m}} < r_{\mathrm{M}} < a, \end{cases}$$

where $F(x) = E_1(x) - \frac{e^{ia}}{2}E_1(x + ia) - \frac{e^{-ia}}{2}E_1(x - ia)$, $z_{M/m} = r_{M/m} - i\sqrt{a^2 - r_{M/m}^2}$, $z_{M,m}^\pm = r_{M/m} \pm \sqrt{r_{M/m}^2 - a^2}$, and $E_1(x)$ is called the exponential integral defined in [80] and is readily available in the Python package [81]. To get the final decoherence function at time τ, we divide the results above by $\ln(r_M/r_m)$ and raise them to the power of N_f. Additionally, when $a = 0$ or $\tau = 0$, some of these terms will diverge; however, as we know that in either of these cases, no dephasing occurs even for a single fluctuator. The decoherence function can safely be set to 1 in either of the cases.

APPENDIX C: DERIVATION OF TWO LIMITS OF EVOLVED DENSITY MATRIX UNDER A SINGLE RTN FLUCTUATOR

In this Appendix, we derive the approximate expressions for the density matrix under RTN dephasing in the two limits of the value of r: $r \ll 1$ and $r \gg 1$. For $r \ll 1$, i.e, where the average switching rate of the fluctuator is smaller than the coupling strength, we see in Sec. II that the evolution of a coherent state has the majority of the contribution coming from two blobs going around the circle for small times. We can understand this behavior by expanding the expression of the dephasing function in order of r. From Eq. (3), we have

$$\begin{aligned}\langle e^{i\phi(m-n)}\rangle_{\phi(\tau)} &= e^{-r\tau}\left(\cos\ |\Omega|\tau + \frac{r}{|\Omega|}\sin\ |\Omega|\tau\right)\\ &= e^{-r\tau}\left(\left(\frac{|\Omega|+r}{2|\Omega|}\right)e^{i|\Omega|\tau}+\left(\frac{|\Omega|-r}{2|\Omega|}\right)e^{-i|\Omega|\tau}\right),\end{aligned} \tag{C1}$$

where $\Omega = \sqrt{(m-n)^2 - r^2}$.

Plugging this into the expression of the evolved density matrix and keeping the terms only up to zeroth order in r, we have

$$\begin{aligned}\hat{\rho}(\tau) = e^{-r\tau}\left(\frac{|\Omega|+r}{2|\Omega|}\right)e^{-|\alpha|^2}\sum_{m,n=0}^{\infty}\frac{(\alpha)^n(\alpha^*)^m e^{i|\Omega|\tau}}{\sqrt{n!m!}}|n\rangle\langle m|\\ + e^{-r\tau}\left(\frac{|\Omega|-r}{2|\Omega|}\right)e^{-|\alpha|^2}\sum_{m,n=0}^{\infty}\frac{(\alpha)^n(\alpha^*)^m e^{-i|\Omega|\tau}}{\sqrt{n!m!}}|n\rangle\langle m|.\end{aligned} \tag{C2}$$

Further for small times when $r\tau \ll 1$, see that $e^{-r\tau} \approx 1$, and the expression becomes

$$\begin{aligned}\hat{\rho}(\tau) = \frac{1}{2}e^{-|\alpha|^2}\sum_{m,n=0}^{\infty}\frac{\alpha_0^n\alpha_0^m e^{i(m-n)(\theta+\tau)}}{\sqrt{n!m!}}|n\rangle\langle m|\\ + \frac{1}{2}e^{-|\alpha|^2}\sum_{m,n=0}^{\infty}\frac{\alpha_0^n\alpha_0^m e^{i(m-n)(\theta-\tau)}}{\sqrt{n!m!}}|n\rangle\langle m|,\end{aligned} \tag{C3}$$

where $\alpha = \alpha_0 e^{i\theta}$. Now, we observe that as a function of τ, the contribution to the evolved state equally comes from two coherent states with their phases shifted by τ. Thus, the Wigner function has two blobs that move around the circle as a function of time. As τ increases, the term $e^{-r\tau}$ can no longer be approximated to be 1, and it begins to give a decaying component to the density matrix. After a long time, the effect of this RTN noise is similar to that of Gaussian noise, where the state is completely dephased.

In the other limit, where we have $r \gg 1, m, n$, we see that the evolved density matrix tends to the case of a Gaussian dephasing of the form $\mathcal{N}_{\sigma^2}\hat{\rho}_0 = \int_{-\infty}^{\infty} d\theta\ p(\theta)e^{-i\theta\hat{n}}\hat{\rho}_0 e^{i\theta\hat{n}}$, where $p(\theta)$ is taken from a Gaussian distribution with standard deviation $\sigma^2 = k_\phi\tau$. For the Gaussian channel, by expanding the density matrix in the Fock basis, and then performing the integral over θ in the above equation, and after completing the squares, we get

$$\begin{aligned}\mathcal{N}_{\sigma^2}\hat{\rho}_0 &= \sum_{m,n=0}^{\infty}\int_{-\infty}^{\infty}d\theta\frac{1}{\sqrt{2\pi\sigma^2}}e^{-\frac{\theta^2}{2\sigma^2}}e^{i\theta(m-n)}\rho_{m,n}|m\rangle\langle n|\\ &= \sum_{m,n=0}^{\infty}\rho_{m,n}|m\rangle\langle n|e^{-\frac{1}{2}(m-n)^2\sigma^2},\end{aligned} \tag{C4}$$

where $\rho_{m,n} = \langle m|\hat{\rho}_0|n\rangle$. We now show how the evolution of the density matrix under RTN with a high switching rate reduces to this result with $\sigma^2 = \tau/r$. In this limit of $r \gg 1, m-n$, we have $\Omega = r(1 - \frac{(m-n)^2}{2r^2})$ and $\cos h\Omega\tau = \sin h\Omega\tau \simeq e^{\Omega\tau}/2$. Up to zeroth order in $\frac{(m-n)^2}{2r^2}$, Eq. (2) becomes

$$\begin{aligned}\hat{\rho}(t) &= \sum_{m,n=0}^{\infty}e^{-r\tau}e^{\Omega\tau}\rho_{m,n}|m\rangle\langle n|\\ &= \sum_{m,n=0}^{\infty}e^{-\frac{1}{2}\frac{(m-n)^2\tau}{r}}\rho_{m,n}|m\rangle\langle n|.\end{aligned} \tag{C5}$$

Comparing this with Eq. (C4), we see that it has a form similar to the evolved Gaussian dephased state with $k_\phi = 1/r$.

APPENDIX D: WIGNER NEGATIVITY—ANOTHER MEASURE OF NON-MARKOVIANITY

Another measure of non-Markovianity based on the Wigner negativity volume also serves as an indicator of the quantum correlations in any composite quantum system [82–86]. In this Appendix, we use Wigner negativity as an alternative metric to further validate our findings regarding the transition between Markovian and non-Markovian regimes for the RTN noise, characterized by the ratio r. The generalized Wigner function negativity volume is defined as [84]

$$N_V = \frac{1}{2}\left[\int dqdp\ |W_{\hat{\rho}}(q,p)| - 1\right], \tag{D1}$$

where $W_{\hat{\rho}}(q,p)$ is the Wigner function defined over the phase space as

$$W_{\hat{\rho}}(q,p) = \frac{1}{\pi}\int_{-\infty}^{\infty}\mathrm{d}y\ e^{2ipy}\langle q+y|\hat{\rho}|q-y\rangle, \tag{D2}$$

where $|q\rangle$ is an eigenstate of the position operator, $\hat{q}$: $\hat{q}|q\rangle = q|q\rangle$.

For Markovian dynamics, the negativity volume is a monotonically decreasing function of time, reflecting the increasing entanglement between the system and the environment. In contrast, non-Markovian dynamics are characterized by an increase in Wigner negativity at certain time intervals. This oscillatory behavior enables the quantification of non-Markovianity based on the Wigner negativity volume. The degree of non-Markovianity $\mathcal{N}_{WN}$ is defined as [87]

$$\mathcal{N}_{WN} = 1 - \frac{\left|\int dt\ \frac{dN_V}{dt}\right|}{\int dt\ \left|\frac{dN_V}{dt}\right|}. \tag{D3}$$

By definition, this measure is zero again for Markovian processes as $\frac{dN_V}{dt} < 0$ for all times.

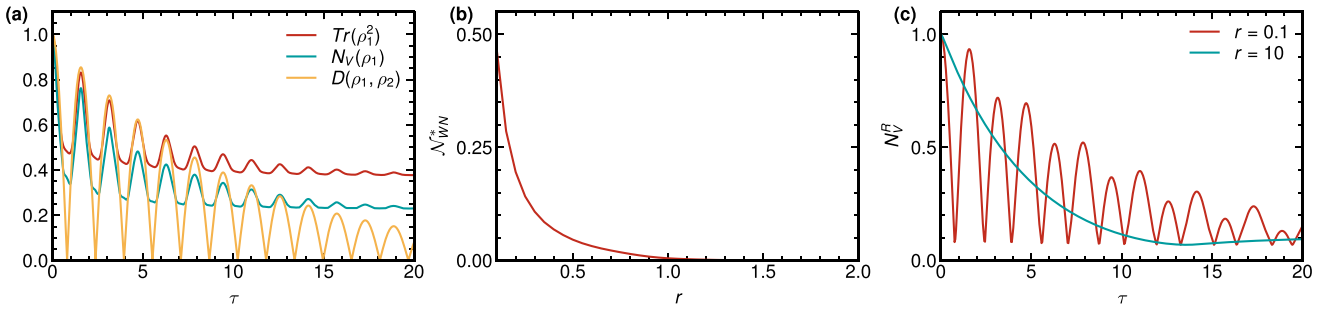

FIG. 8. (a) The Wigner negativity exhibits oscillations with τ for a binomial state $|+\rangle_{2,2}$ in the non-Markovian regime where $r = 0.1$. The period of oscillations of Wigner negativity is the same as that of the purity of $|+\rangle_{2,2}$ and the trace distance between states $|+\rangle_{2,2}$ and $|-\rangle_{2,2}$. (b) We plot the measure of non-Markovianity based on Wigner negativity N^*_{WN} for the same state $|+\rangle_{2,2}$ as a function of the ratio of r. The asterisk in the superscript indicates that this measure is not maximized over a set of states, but is specific to a given state. From this measure, we see the bosonic mode transits from a non-Markovian to a Markovian regime close to $r = 1$. (c) The plot shows Wigner negativity integrated only along a ring at radius $R = 1.2$ for $|+\rangle_{1,2}$ in the phase space, and we again observe oscillations in the non-Markovian regime and a monotonic decay in the Markovian regime.

From an experimental perspective, studying Wigner negativity offers significant advantages. Its evolution is easier to probe and measure compared to the $\mathcal{N}_{\mathrm{BLP}}$ measure of non-Markovianity, making it a practical choice for experimental validation of non-Markovian effects. In Fig. 8(a), we plot the evolution of the Wigner negativity as given in Eq. (D1) for a so called binomial state $|+\rangle_{2,2}$. The definition of binomial states has been provided in the subsequent section in Appendix F. In the non-Markovian regime when $r = 0.1$, we see revivals of N_V, while for $r = 10$, the function monotonically decays. The period of oscillations of N_V is the same as the period of revivals of the trace distance for the same state with $|-\rangle_{2,2}$. However, we notice that the Wigner negativity tends to a constant value faster than the trace distance approaches zero. We plot this in Fig. 8(b) and as expected the measure exponentially reduces as a function of r approaching the Markovian limit. Further, to facilitate the study of the behavior of the Wigner negativity experimentally, we also look at the Wigner function integrated over a ring of radius $\sqrt{p^2+q^2} = R$ in the phase space. We define this quantity $N_V(R)$ as follows:

$$N_V^R = \frac{1}{2}\left[\int d\theta\ |W_{\hat{\rho}}(R,\theta)| - 1\right], \tag{D4}$$

where $R = \sqrt{p^2+q^2}$ and $\theta = \tan^{-1}\frac{p}{q}$. In Fig. 8(c), we plot Wigner negativity along a ring of radius $R = 1.2$ for a binomial state $|+\rangle_{1,2}$ as a function of time. The difference in behavior in the non-Markovian and the Markovian limits is evident even when integrated only along a ring; the radius of the ring has to be chosen in accordance with the given initial state, such that the Wigner negativity is finite.

APPENDIX E: OPTIMIZATION OF NON-MARKOVIAN MEASURE FOR GAUSSIAN STATES

In this Appendix, we elaborate on the optimization procedure of the non-Markovian measure for Gaussian states. As discussed in Sec. III A, a general Gaussian state is described by two complex parameters α and β and one real parameter $\tilde{N}$ [see Eq. (13)]. To find the value of $\mathcal{N}_{\mathrm{BLP}}$ for the subset of Gaussian states, we need to maximize over two initial states and thus over the following ten parameters: $(\alpha_{0_1}, \alpha_{0_2}, \theta_1, \theta_2, \beta_{0_1}, \beta_{0_2}, \gamma_1, \gamma_2, \tilde{N}_1, \tilde{N}_2)$. We observe that for certain relations between these parameters, the non-Markovian measure is maximum and gives the same value for a set of these parameters. By fixing the parameters of the first state, we see that the parameters of the second state satisfying the following conditions give the maximum value of $\mathcal{N}^*_{\mathrm{BLP}}$ [Figs. 9(a), 9 (b), 9 (d), and 9 (e)],

$$\begin{aligned}
\alpha_{0_2} &= \alpha_{0_1},\\
\theta_2 &= \pm\pi - \theta_1,\\
\beta_{0_2} &= \beta_{0_1},\\
\gamma_2 &= \gamma_1,\\
\tilde{N}_2 &= \tilde{N}_1.
\end{aligned} \tag{E1}$$

The value of the measure is the same for any choice of the parameters θ_2 and γ_2 that satisfy the above conditions. Thus the optimization problem reduces to considering three parameters $\alpha_{1_0} = \alpha_{2_0} = \alpha_0$, $\beta_{1_0} = \beta_{2_0} = \beta$, and $\tilde{N}_1 = \tilde{N}_2 = \tilde{N}$. Further, as a function of the squeezing amplitude and the average photon number, we observe that the maximum value of $\mathcal{N}^*_{\mathrm{BLP}}$ scanning over all states is obtained for a pair of coherent states with a particular value of α_0 depending on the ratio r with no squeezing and no thermal fluctuations, respectively [shown in Figs. 2(b), 9(f), and 9(c)].

APPENDIX F: CONSTRUCTION OF RSB CODES

In this Appendix, we elaborate on the construction of RSB codes. A code exhibits discrete N-fold rotational symmetry if every state in its code space is an eigenstate of the discrete rotation operator [27]

$$\hat{R}_N = e^{i\frac{2\pi}{N}\hat{n}}, \tag{F1}$$

with eigenvalue $+1$. We also define a logical $\hat{Z}_N$ operator as the square root of $\hat{R}_N$, which also preserves the rotational symmetry,

$$\hat{Z}_N = \hat{R}_{2N} = e^{i\frac{\pi}{N}\hat{n}}. \tag{F2}$$

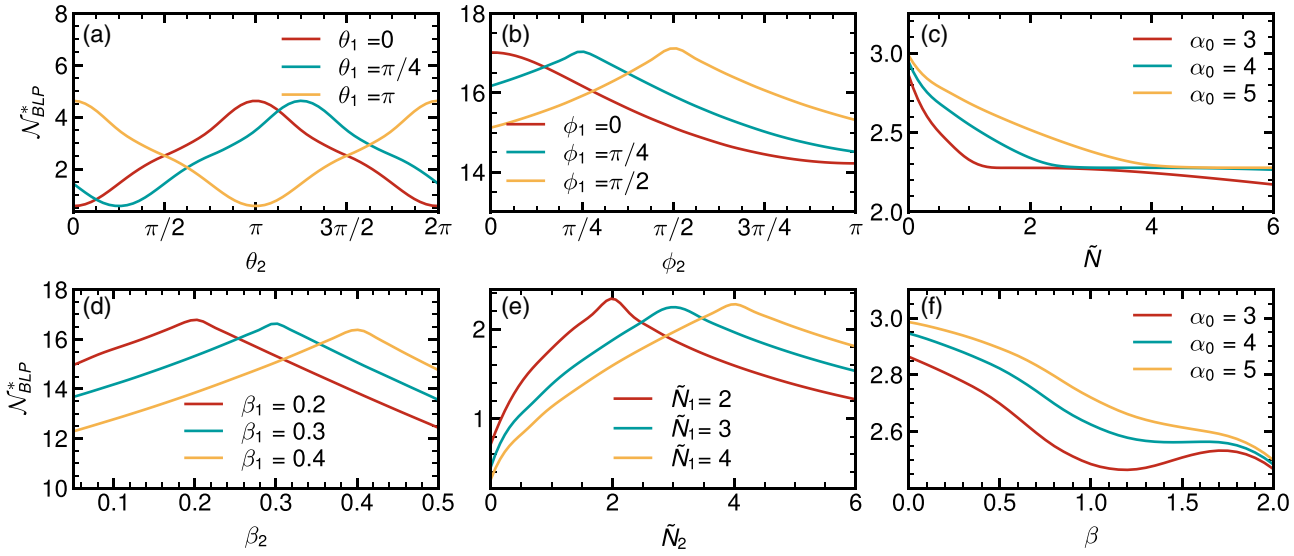

FIG. 9. The optimization procedure consists of maximizing over the following ten parameters: $(\alpha_{0_1}, \alpha_{0_2}, \theta_1, \theta_2, \beta_{0_1}, \beta_{0_2}, \gamma_1, \gamma_2, \tilde{N}_1, \tilde{N}_2)$. We see that for different values of the maxima in the plots occur at (a) $|\theta_1 - \theta_2| = \pi$, (b) $\phi_1 = \phi_2$, (d) $\beta_1 = \beta_2$, and (e) $\tilde{N}_1 = \tilde{N}_2$. Further in panels (c) and (f), we see that squeezing and thermal excitations do not increase the value of $\mathcal{N}_{\text{BLP}}$.

As such, N-order RSB code is characterized by $\pm$ eigenvalue of the logical $\hat{Z}_N$ on the codespace, represented by the projector $\hat{\Pi}_{\text{code}} = |0\rangle\langle 0|_{\text{code}} + |1\rangle\langle 1|_{\text{code}}$.

Given that the logical code words $|0\rangle_N$ and $|1\rangle_N$ satisfy the eigenvalue condition $\hat{Z}_N|j\rangle_N = (-1)^j|j\rangle_N$ for $j \in 0, 1$, they can be constructed from discrete rotated superpositions of a primitive state $|\Theta\rangle$ such that

$$|0\rangle_{N,\Theta} = \frac{1}{\sqrt{N_0}} \sum_{m=0}^{2N-1} e^{i\frac{m\pi}{N}\hat{n}}|\Theta\rangle, \tag{F3}$$

$$|1\rangle_{N,\Theta} = \frac{1}{\sqrt{N_1}} \sum_{m=0}^{2N-1} (-1)^m e^{i\frac{m\pi}{N}\hat{n}}|\Theta\rangle, \tag{F4}$$

where N_i are the normalization constants. By expressing the primitive state in Fock basis as $|\Theta\rangle = \sum_n c_n|n\rangle$, the code words can be written as

$$|0\rangle_N = \sum_k f_{2kN}|2kN\rangle, \tag{F5}$$

$$|1\rangle_N = \sum_k f_{(2k+1)N}|(2k+1)N\rangle, \tag{F6}$$

where f_{kN} are coefficients determined by the primitive state. In the dual basis, the code words transform into

$$|\pm\rangle_N = \frac{1}{\sqrt{2}}(|0\rangle_N + |1\rangle_N) = \frac{1}{\sqrt{2}} \sum_k^{\infty} (\pm 1)^k f_{kN}|kN\rangle. \tag{F7}$$

This implies that, for the code words to be well defined, the primitive state must have nonzero support on at least one of the $|2kN\rangle$ and one of the $|2kN + 1\rangle$ states. In this work, we have focused on binomial codes and cat codes. For cat codes, the computational code words $|0_N\rangle$ and $|1_N\rangle$ are constructed by taking the primitive state in Eq. (F4) as the coherent states, $|\Theta\rangle = |\alpha\rangle = e^{-|\alpha|^2/2}\sum_n \alpha^n/\sqrt{n!}|n\rangle$. The rotated superpositions of these states form the code words as

$$|0\rangle_N = \frac{1}{\sqrt{N_0}} \sum_{m=0}^{2N-1} \left|\alpha e^{i\frac{m\pi}{N}}\right\rangle, \tag{F8}$$

$$|1\rangle_N = \frac{1}{\sqrt{N_1}} \sum_{m=0}^{2N-1} (-1)^m \left|\alpha e^{i\frac{m\pi}{N}}\right\rangle. \tag{F9}$$

For the class of binomial codes, the code words have the following form, with the coefficients f_{kN} given by binomial distribution [27,88]:

$$|0\rangle_{N,K} = \sum_{k=0}^{\lfloor K/2 \rfloor} \sqrt{\frac{1}{2^{K-1}}\binom{K}{2k}}|2kN\rangle, \tag{F10}$$

$$|1\rangle_{N,K} = \sum_{k=0}^{\lceil K/2-1 \rceil} \sqrt{\frac{1}{2^{K-1}}\binom{K}{2k+1}}|(2k+1)N\rangle. \tag{F11}$$

These codes can correct against photon losses, photon gains, and dephasing. The parameter K is the truncation limit and determines the maximum order up to which the code can correct for the above-mentioned errors.

APPENDIX G: $\mathcal{N}_{\text{BLP}}$ MEASURE FOR NON-GAUSSIAN STATES

In this Appendix, we show that going beyond the Gaussian states, one can find a limiting case, where a pair of non-Gaussian states will yield an integrated revival of trace distance, which is unbounded from above. To see this, let us take the subspace H_l spanned by the Fock states $\{|0>, |l>\}$ of the infinite dimensional Hilbert space, comprising of all normalized linear combinations of the Fock states $\{|0\rangle, |l\rangle\}$. In the non-Markovian regime of RTN, any state belonging to the space $\mathcal{S}(H_l)$ will undergo decoherence exactly like a qubit

but with a dephasing factor given by

$$G(l,\tau) = e^{-r\tau}\left(\cosh\Omega_l\tau + \frac{r}{\Omega_l}\sinh\Omega_l\tau\right), \tag{G1}$$

where $\Omega_l = \sqrt{r^2 - l^2}$. As it has been shown in Ref. [89], the trace distance for the optimal pair of qubit states (which maximizes $\mathcal{N}_{\mathrm{BLP}}$) evolves as $D(\tau) = |G(l,\tau)|$. The revival of the trace distance, quantified as the cumulative sum of the trace distance between two specific states for all the time intervals during which the trace distance is increasing can be calculated and is given by

$$N_l = \sum_{n=1}^{\infty} \left|G\left(l, T_l^n\right)\right|, \tag{G2}$$

where $T_l^n = n\pi/\Omega_l$ is the time when the nth maximum of $|G(l,\tau)|$ occurs (the minima are all zero). This geometric series yields

$$N_l = \frac{1}{e^{\pi r/\Omega_l} - 1}. \tag{G3}$$

For every r, in the limit $l \to \infty$, $N_l \to \infty$. Hence, the BLP measure for RTN affecting a bosonic system is unbounded.

APPENDIX H: DERIVATION OF THE RECOVERY MAP OF KNILL ERROR-CORRECTION CIRCUIT

In this Appendix, we review the details of Knill error-correction circuit given in Ref. [27] and derive the resulting recovery channel. To our knowledge, this derivation has not been documented before. Referring back to the circuit in Fig. 4, it includes the preparation of $|+\rangle_N$ states, crot gates (controlled rotations) that act as logical controlled-Z gates on encoded code words, and measurements to distinguish logical code words in the dual basis.

The input state of the three modes has the following form:

$$\mathcal{N}_N \otimes \mathbb{1}_{ML}(\hat{\rho}_N \otimes |+\rangle\langle+|_M \otimes |+\rangle\langle+|_L), \tag{H1}$$

where $\mathbb{1}_{ab}$ is the identity operator acting on the modes a and b, and $\mathcal{N}_N$ is the map of the noise channel acting on order-N input mode. We henceforth omit the identity operator, and it is understood by context on the modes it acts on. Here, the input state in the computational code basis is given by $\hat{\rho}_N = \sum_{p,q=0}^{1} \rho_{p,q}|p\rangle_N\langle q|_N$.

The crot gate is given by

$$\mathrm{CROT}_{NM} = e^{i(\pi/NM)\hat{n}_a\otimes\hat{n}_b}, \tag{H2}$$

and serves as a logical controlled-Z gate, acting on the code words as $\mathrm{CROT}_{NM}|i\rangle_N \otimes |j\rangle_M = (-1)^{ij}|i\rangle_N \otimes |j\rangle_M$. The number-shift errors in one mode propagate as rotation errors in the other, and we see that this feature is crucial to obtaining the recovery map for the noisy state.

To distinguish logical code words in a dual basis, we employ a phase-sensitive POVM [69]:

$$\hat{M}(\phi) = \frac{1}{2\pi}\sum_{m,n=0}^{\infty} e^{i\phi(m-n)}B_{mn}|m\rangle\langle n|, \tag{H3}$$

where B is a positive semidefinite Hermitian matrix and $\phi \in [0, 2\pi)$. We primarily use canonical phase measurements for which $B_{mn} = 1$ [69].

The state, after passing through the two controlled rotation gates, is

$$\hat{C}_{ML}\hat{C}_{NM}\mathcal{N}_N(\hat{\rho}_N|+\rangle\langle+|_M|+\rangle\langle+|_L)\hat{C}_{NM}^{\dagger}\hat{C}_{ML}^{\dagger}, \tag{H4}$$

where $\hat{C}_{NM}$ denotes the crot gate acting on modes of order N and order M. Inserting $\hat{C}_{NM}\hat{C}_{NM}^{\dagger}$, we can rewrite the above equation as follows:

$$\hat{C}_{ML}\overbrace{\hat{C}_{NM}\mathcal{N}_N\hat{C}_{NM}^{\dagger}\underbrace{\hat{C}_{NM}\hat{\rho}_N|+\rangle\langle+|_M|+\rangle\langle+|_L\hat{C}_{NM}^{\dagger}}_{\hat{A}(\hat{\rho})}\hat{C}_{NM}\hat{C}_{NM}^{\dagger}}^{\hat{B}(\hat{\rho})}\hat{C}_{ML}^{\dagger}, \tag{H5}$$

where we have used $\hat{\rho}_N = \sum_{p,q=0}^{1}\rho_{p,q}|p\rangle_N\langle q|_N$.

By looking at the action of $\hat{C}_{NM}$ on the input states, we can evaluate the term $\hat{A}(\hat{\rho})$. We have

$$\hat{C}_{NM}|p\rangle_N|+\rangle_M = |p\rangle_N|h^p\rangle_M, \tag{H6}$$

where $|h^0\rangle_M = |+\rangle_M$ and $|h^1\rangle_M = |-\rangle_M$ for $p = 0$ and $p = 1$, respectively. Thus, we have

$$\hat{A}(\hat{\rho}) = \sum_{p,q=0}^{1}\rho_{p,q}|p\rangle\langle q|_N|h^p\rangle\langle h^q|_M|+\rangle\langle+|_L. \tag{H7}$$

Next, we look at the term $\hat{B}(\hat{\rho})$, and implementing the action of the noise channel in terms of the Kraus operators for both loss and dephasing $\hat{K}_l$ and $\hat{K}_d$, respectively, we have

$$\begin{aligned}\hat{B}(\hat{\rho}) &= \hat{C}_{NM}\mathcal{N}(\hat{C}_{NM}^{\dagger}\hat{A}(\hat{\rho})\hat{C}_{NM})\hat{C}_{NM}^{\dagger}\\ &= \sum_{l,d}\hat{K}_d\hat{K}_l\hat{R}_M\hat{A}(\hat{\rho})\hat{R}_M^{\dagger}\hat{K}_l{}^{\dagger}\hat{K}_d{}^{\dagger},\end{aligned} \tag{H8}$$

where we have used the fact that crot gate commutes with the dephasing Kraus operator and gives an additional rotational operation $\hat{R}_M$ on the second mode when it is commuted through the loss Kraus operator [27]. The angle of this rotation operator depends on the index l of the loss Kraus operator [27]. The final equation thus gives,

$$\hat{C}_{ML}\hat{B}(\hat{\rho})\hat{C}_{ML}^{\dagger} = \sum_{l,d}\hat{K}_d\hat{K}_l\hat{R}_M\hat{C}_{ML}\hat{A}(\hat{\rho})\hat{C}_{ML}^{\dagger}\hat{R}_M^{\dagger}\hat{K}_l{}^{\dagger}\hat{K}_d{}^{\dagger}, \tag{H9}$$

where we have used the fact that the operator $\hat{C}_{ML}$ does not act on the order-N mode, it commutes through the Kraus and the error operators.

We now look at the action of $\hat{C}_{ML}$ on the state for $p = 0$ and $p = 1$, and using Pauli operators acting on the order-L state, we see that

$$\begin{aligned}\hat{C}_{ML}|0,+,+\rangle &= \tfrac{1}{2}(|+,+\rangle\mathbb{1} + |-,+\rangle\hat{Z}\\ &\quad + |+,-\rangle\hat{X} + |-,-\rangle\hat{X}\hat{Z})|0\rangle_L,\\ \hat{C}_{ML}|1,-,+\rangle &= \tfrac{1}{2}(|+,+\rangle\mathbb{1} + |-,+\rangle\hat{Z}\\ &\quad + |+,-\rangle\hat{X} + |-,-\rangle\hat{X}\hat{Z})|1\rangle_L,\end{aligned} \tag{H10}$$

where $|a,b,c\rangle = |a\rangle_N|b\rangle_M|c\rangle_L$, with $a, b, c = 0, 1, \pm$.

Using the following notation, $|0\rangle = |+,+\rangle$, $|1\rangle = |+,-\rangle$, $|2\rangle = |-,+\rangle$, and $|3\rangle = |-,-\rangle$ for the states, and

$\hat{P}_i \in \{\mathbb{I}, \hat{X}, \hat{Z}, \hat{X}\hat{Z}\}$, we get

$$\hat{C}_{ML}\hat{A}(\hat{\rho})\hat{C}_{ML}^{\dagger} = \frac{1}{4}\sum_{i,j=0}^{3} |i\rangle\langle j|\hat{P}_i\hat{\rho}_L\hat{P}_j^{\dagger}. \tag{H11}$$

Thus, finally Eq. (H9) after measurement of $\hat{M}_{x_1}$ and $\hat{M}_{x_2}$, and summing over all the values of x_1 and x_2, becomes

$$\hat{\rho}_{\text{out}} = \frac{1}{4}\sum_{x_1,x_2}\sum_{i,j=0}^{3} c_{ij}(\vec{x})\hat{P}_i\hat{\rho}_L\hat{P}_j^{\dagger}, \tag{H12}$$

where $c_{ij} = \text{Tr}(\hat{M}_{x_1} \otimes \hat{M}_{x_2}(\hat{\mathcal{U}}_c \circ \mathcal{N} \circ \hat{\mathcal{U}}_c^{\dagger}|i\rangle\langle j|))$ and $\hat{\mathcal{U}}_c \circ = \hat{C}_{NM} \circ \hat{C}_{NM}^{\dagger}$.

APPENDIX I: DERIVATION OF AVERAGE GATE FIDELITY FOR A PURELY DEPHASING CHANNEL

Here, we include the derivation of the average gate fidelity of the recovery map in the Knill EC in the presence of a purely dephasing map and an arbitrary rotation-symmetric bosonic encoding. The $c_{ij}(x_1, x_2)$ matrices, given in the previous section, for a canonical phase measurement [where we have set the elements of the matrix B in Eq. (H3) to 1] can be explicitly written as

$$\begin{aligned} &c_{ij}(\phi_1, \phi_2) \\ &= \frac{1}{2\pi}\sum_{k,l=0}^{\infty}(-1)^{ka+lc} f_{kN}\, f^*_{lN}\, G(kN, lN, \tau)\, e^{i(l-k)N\phi_1} \\ &\quad\times \frac{1}{2\pi}\sum_{k,l=0}^{\infty}(-1)^{kb+ld} g_{kM}\, g^*_{lM}\, e^{i(l-k)M\phi_2}, \end{aligned} \tag{I1}$$

where ab and cd are the binary representations of i and j, respectively. The f and g are the binomial coefficients of the code words, and the phases ϕ_1 and ϕ_2 are the measurements on the order-N and order-M code, respectively. $G(kN, lN, r, \tau)$ is the dephasing function with the kN and lN being the indexes of the Fock basis running over the integers. The average gate fidelity for a qubit system ($d = 2$) is given by [72]

$$\mathcal{F} = \frac{\text{Tr}[\mathcal{E}(\mathbb{I})] + \text{Tr}[\hat{X}\mathcal{E}(\hat{X})] + \text{Tr}[\hat{Z}\mathcal{E}(\hat{Z})] + \text{Tr}[\hat{Z}\hat{X}\mathcal{E}(\hat{X}\hat{Z})] + 4}{12}, \tag{I2}$$

where $\mathcal{E}$ is the map given in Eq. (15). Replacing the sum over $x_i's$ with integrals over $\phi_i's$ in this equation, we evaluate the contribution from each of these terms to the fidelity. The first term $\text{Tr}[\mathcal{E}(\mathbb{I})]$ trivially simplifies to 2. The second term can be computed as follows:

$$\begin{aligned} \text{Tr}[\hat{X}\mathcal{E}(\hat{X})] = \frac{1}{4}\int \text{d}\phi_1\text{d}\phi_2 (c_{00}(\vec{\phi}) + c_{11}(\vec{\phi}) - c_{22}(\vec{\phi}) - c_{33}(\vec{\phi})) \\ \times \text{Tr}\big[\hat{X}\hat{P}^{L\dagger}_{i*(\vec{\phi})}\hat{X}\hat{P}^{L}_{i*(\vec{\phi})}\big]. \end{aligned} \tag{I3}$$

Writing i as the binary equivalent $i \equiv ab$, we have

$$c_{ii}(\vec{\phi}) = c_a^{\tau}(\phi_1) \times c_b(\phi_2),$$

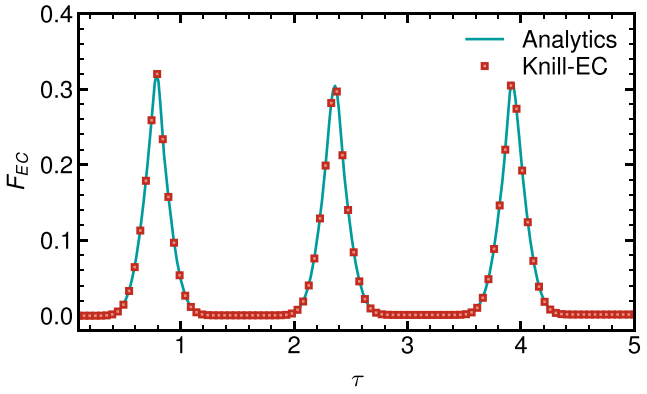

FIG. 10. The analytical expression for the average gate fidelity of the circuit compared with the same obtained from the numerical realization of the error-correction circuit.

where $c_a^{\tau}(\phi_1) = \text{Tr}\{\hat{M}(\phi_1)\mathcal{N}(|(-)^a\rangle\langle(-)^a|_N)\}$ and $c_b(\phi_2) = \text{Tr}\{\hat{M}(\phi_2)(|(-)^b\rangle\langle(-)^b|_M))\}$. This allows us to rewrite

$$(c_{00} + c_{11} - c_{22} - c_{33})(\vec{\phi}) = \big(c_0^{\tau} - c_1^{\tau}\big)(\phi_1)(c_0 + c_1)(\phi_2). \tag{I4}$$

When $i^*(\vec{\phi}) \in \{0, 1\}$, the trace in Eq. (I3) evaluates to 2 and $c_0^{\tau}(\phi_1) > c_1^{\tau}(\phi_1)$, otherwise the trace evaluates to -2 and $c_1^{\tau}(\phi_1) > c_0^{\tau}(\phi_1)$. Putting these together and performing the integral over ϕ_2, which evaluates to 1, the expression simplifies to

$$\text{Tr}[\hat{X}\mathcal{E}(\hat{X})] = \int_0^{2\pi} \text{d}\phi_1 \ \big|c_0^{\tau} - c_1^{\tau}\big|(\phi_1). \tag{I5}$$

A similar analysis shows that

$$\text{Tr}[\hat{Z}\mathcal{E}(\hat{Z})] = \int_0^{2\pi} \text{d}\phi_2 \ |c_0 - c_1|(\phi_2), \tag{I6}$$

where we have assumed the noise is trace-preserving while evaluating the integral over ϕ_1. We also have

$$\begin{aligned} \text{Tr}[\hat{Z}\hat{X}\mathcal{E}(\hat{X}\hat{Z})] = \frac{1}{2}\int_0^{2\pi} \text{d}\phi_1 \ \big|c_0^{\tau} - c_1^{\tau}\big|(\phi_1) \\ \times \int_0^{2\pi} \text{d}\phi_2 \ |c_0 - c_1|(\phi_2). \end{aligned} \tag{I7}$$

We substitute these into Eq. (I2) to get the final expression for fidelity of the error-corrected map. In Fig. 10, we compare the results from the values of $\mathcal{F}_{\text{EC}}$ obtained from the error circuit and the values from the integrals of the expression above, and find that they agree well. We note that for the final expressions, we can conveniently generalize them for any measurement scheme by keeping the elements of matrix B throughout the proof. To infer the time dependence of the fidelity, it is sufficient to analyze $\int_0^{2\pi} \text{d}\phi_1 \ |c_0^{\tau} - c_1^{\tau}|(\phi_1)$ for a canonical measurement. For a binomial code with $K = 2$ and

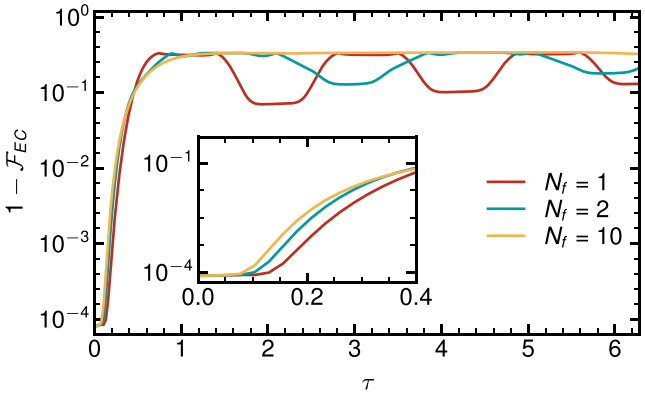

FIG. 11. The performance of the binomial codes with $N = 3$ and $K = 8$ under the same $1/f$ noise as a function of τ. We see oscillations that decay as N_f increases. The behavior for initial times is shown in the inset, where the infidelity is lower for smaller values of N_f.

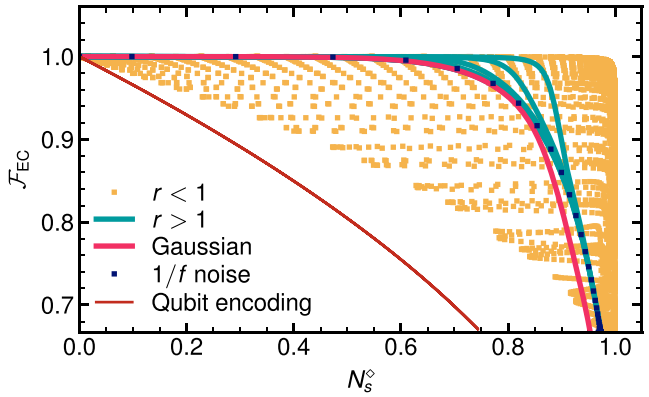

FIG. 12. The performance of the cat codes with $N = 2$ and $\alpha^2 = 12$ under different dephasing channels as a function of the noise strength of the channel. We also plot the qubit encoding, which is a trivial encoding of information in the $|0\rangle$ and $|1\rangle$ Fock states.

arbitrary N, we see that the quantity

$$\int_0^{2\pi} d\phi_1 \left|c_0^\tau - c_1^\tau\right|(\phi_1) = \frac{4}{2\pi}\int_0^{2\pi} d\phi_1 \left|(f_0 f_N + f_N f_{2N}) G(0,N,\tau)\cos(N\phi_1)\right| = \frac{4\sqrt{2}}{\pi}|G(0,N,\tau)| \tag{I8}$$

oscillates with the frequency $\Omega = 2\sqrt{N^2 - r^2}$. This matches the numerical simulation as well, where we observe the frequency of oscillations increase linearly with N. To illustrate what happens for higher K, let us take the example of $K = 3$, for which the integral becomes

$$\int_0^{2\pi} d\phi_1 \left|c_0^\tau - c_1^\tau\right|(\phi_1) = \frac{4}{2\pi}\int_0^{2\pi} d\phi \left|F_1 G(0,N,\tau)\cos(\phi) + F_3 G(3N,t)\cos(3\phi)\right|, \tag{I9}$$

where $F_1 = (1/8)(2\sqrt{3}+3)$ and $F_3 = (1/8)$. We see that we have a higher contribution from $G(N,t)$ than from $G(3N,t)$, dominating the time dependence of fidelity, however, with a higher width of the maxima and a lesser value of minima. With higher values of K, this trend seems to be continuing as we checked numerically (see Fig. 10). However, when we include the loss channel, we encounter a trade-off since, with increasing K, the average excitation number also increases, leading to a higher photon loss rate.

We further find a bound on the value of the fidelity for a pure dephasing channel. We note the following well-known inequality relating the distinguishability of states inferred from measurement outcomes to the trace distance between them [76]. For a pair of state, $\hat{\rho}, \hat{\sigma}$, the l_1 distance between the probability distributions, $\{p_m := \mathrm{Tr}(\hat{E}_m\hat{\rho})\}$ and $\{q_m := \mathrm{Tr}(\hat{E}_m\hat{\sigma})\}$, for any set of POVMs, $\{\hat{E}_m\}$, is bounded from above by the trace distance between the two states:

$$\frac{1}{2}\sum_m |p_m - q_m| \leqslant D(\hat{\rho},\hat{\sigma}). \tag{I10}$$

In the present case, $\hat{\rho} \equiv \mathcal{N}(|+\rangle\langle+|)$ and $\hat{\sigma} \equiv \mathcal{N}(|-\rangle\langle-|)$. c_0^τ and c_1^τ are the probability distribution of outcomes corresponding to any set of POVMs (here phase measurements, $\{\hat{M}(\phi) : \phi \in [0, 2\pi)\}$) that is used to distinguish the dual code words that are going through the noisy channel, $\mathcal{N}$. Therefore, we have

$$\int_0^{2\pi} d\phi_1 \left|c_0^\tau - c_1^\tau\right|(\phi_1) \leqslant 2D(|+\rangle_N, |-\rangle_N), \tag{I11}$$

where we note that $D(|+\rangle_N, |-\rangle_N$ depends on τ. As we have observed that the trace distance of the dual code words of any rotation-symmetric bosonic encoding exhibits an oscillation with sharp dips, the corresponding dips in the fidelity of the Knill EC are also fundamentally bounded from above. Explicitly,

$$\mathcal{F}(\tau) \leqslant \frac{2 + [1 + D(|+\rangle_N, |-\rangle_N)][1 + D(|+\rangle_M, |-\rangle_M)]}{6}, \tag{I12}$$

where we once again note that $D(|+\rangle_N, |-\rangle_N$ depends on τ. In Fig. 6(c), we compare this bound to the numerical results of the fidelity obtained from the circuit.

APPENDIX J: PERFORMANCE UNDER $1/f$ NOISE

Here, we present the numerical results of the performance of the binomial encoding subjected to $1/f$ noise dephasing. We use the Knill EC circuit with canonical measurements fixing the binomial encoding to be $N = 3$ and $K = 8$ under $1/f$ noise for the count of fluctuators $N_f = 1, 2$, and 10. In Fig. 11, we see that the infidelity shows oscillations for small values of N_f displaying non-Markovian features and becomes monotonic for $N_f = 10$ as a function of τ, as expected. This is in agreement with Fig. 3(c) where we see that the oscillations in the trace distance for a given pair of binomial states die out, as $N_f \approx 10$.

APPENDIX K: FIDELITY AS A FUNCTION OF NOISE STRENGTH FOR CAT ENCODING

In this Appendix, we provide an additional plot corresponding to the study done in Sec. IV B for fidelity of the Knill EC circuit subjected to different dephasing channels. In Fig. 12, we show fidelity as a function of noise strength, $N_s^{\diamond}$ as defined in Eq. (19) subjected to RTN dephasing, Gaussian dephasing and 1/f noise for cat encoding with $N = 2$ and $\alpha^2 = 12$. The performance is similar to the case shown in the main text for binomial encoding, where we observe that in the non-Markovian limit for $r < 1$, we obtained highly nonmonotonic behavior with orange dots scattered around where as we observe monotonic decrease in fidelity with noise strength for the case where $r > 1$. This is similar to the Gaussian channel (shown in pink in Fig. 12), which also coincides with the $1/f$ channel with ten number of fluctuators. We also have verified that the corresponding plots for infidelity as a function of r for different noise strengths show similar behavior as in Figs. 7(b) and 7(c) for binomial encoding.

[1] K. Noh and C. Chamberland, Fault-tolerant bosonic quantum error correction with the surface–Gottesman-Kitaev-Preskill code, Phys. Rev. A **101**, 012316 (2020).

[2] I. Tzitrin, T. Matsuura, R. N. Alexander, G. Dauphinais, J. E. Bourassa, K. K. Sabapathy, N. C. Menicucci, and I. Dhand, Fault-tolerant quantum computation with static linear optics, PRX Quantum **2**, 040353 (2021).

[3] A. L. Grimsmo and S. Puri, Quantum error correction with the Gottesman-Kitaev-Preskill code, PRX Quantum **2**, 020101 (2021).

[4] M. V. Larsen, *et al.*, Integrated photonic source of Gottesman–Kitaev–Preskill qubits, Nature (London) **642**, 587 (2025).

[5] E. Gouzien, D. Ruiz, F.-M. Le Régent, J. Guillaud, and N. Sangouard, Performance analysis of a repetition cat code architecture: Computing 256-bit elliptic curve logarithm in 9 hours with 126 133 cat qubits, Phys. Rev. Lett. **131**, 040602 (2023).

[6] J. Guillaud and M. Mirrahimi, Repetition cat qubits for fault-tolerant quantum computation, Phys. Rev. X **9**, 041053 (2019).

[7] A. S. Darmawan, B. J. Brown, A. L. Grimsmo, D. K. Tuckett, and S. Puri, Practical quantum error correction with the XZZX code and Kerr-cat qubits, PRX Quantum **2**, 030345 (2021).

[8] M.-A. Lemonde, D. Lachance-Quirion, G. Duclos-Cianci, N. E. Frattini, F. Hopfmueller, C. Gauvin-Ndiaye, J. Camirand-Lemyre, and P. St-Jean, Hardware-efficient fault tolerant quantum computing with bosonic grid states in superconducting circuits, arXiv:2409.05813.

[9] H. A. Rad, T. Ainsworth, R. Alexander, B. Altieri, M. Askarani, R. Baby, L. Banchi, B. Baragiola, J. Bourassa, R. Chadwick, *et al.*, Scaling and networking a modular photonic quantum computer, Nature (London) **638**, 912 (2025).

[10] B. W. Walshe, B. Q. Baragiola, H. Ferretti, J. Gefaell, M. Vasmer, R. Weil, T. Matsuura, T. Jaeken, G. Pantaleoni, Z. Han, T. Hillmann, N. C. Menicucci, I. Tzitrin, and R. N. Alexander, Linear-optical quantum computation with arbitrary error-correcting codes, Phys. Rev. Lett. **134**, 100602 (2025).

[11] C. T. Hann, K. Noh, H. Putterman, M. H. Matheny, J. K. Iverson, M. T. Fang, C. Chamberland, O. Painter, and F. G. S. L. Brandão, Hybrid cat-transmon architecture for scalable, hardware-efficient quantum error correction PRX Quantum **6**, 030305 (2025).

[12] V. Sivak, A. Eickbusch, B. Royer, S. Singh, I. Tsioutsios, S. Ganjam, A. Miano, B. Brock, A. Ding, L. Frunzio, *et al.*, Real-time quantum error correction beyond break-even, Nature (London) **616**, 50 (2023).

[13] Z. Ni, S. Li, X. Deng, Y. Cai, L. Zhang, W. Wang, Z.-B. Yang, H. Yu, F. Yan, S. Liu, *et al.*, Beating the break-even point with a discrete-variable-encoded logical qubit, Nature (London) **616**, 56 (2023).

[14] H. Putterman, *et al.*, Hardware-efficient quantum error correction via concatenated bosonic qubits, Nature (London) **638**, 927 (2025).

[15] A. Marquet, A. Essig, J. Cohen, N. Cottet, A. Murani, E. Albertinale, S. Dupouy, A. Bienfait, T. Peronnin, S. Jezouin, R. Lescanne, and B. Huard, Autoparametric resonance extending the bit-flip time of a cat qubit up to 0.3 s, Phys. Rev. X **14**, 021019 (2024).

[16] U. Réglade, A. Bocquet, R. Gautier, J. Cohen, A. Marquet, E. Albertinale, N. Pankratova, M. Hallén, F. Rautschke, L.-A. Sellem, P. Rouchon, A. Sarlette, M. Mirrahimi, P. Campagne-Ibarcq, R. Lescanne, S. Jezouin, and Z. Leghtas, Quantum control of a cat qubit with bit-flip times exceeding ten seconds, Nature (London) **629**, 778 (2024).

[17] R. Rousseau, *et al.*, Enhancing dissipative cat qubit protection by squeezing, arXiv:2502.07892.

[18] B. L. Brock, S. Singh, A. Eickbusch, V. V. Sivak, A. Z. Ding, L. Frunzio, S. M. Girvin, and M. H. Devoret, Quantum error correction of qudits beyond break-even, Nature (London) **641**, 612 (2025).

[19] C. Flühmann, T. L. Nguyen, M. Marinelli, V. Negnevitsky, K. Mehta, and J. Home, Encoding a qubit in a trapped-ion mechanical oscillator, Nature (London) **566**, 513 (2019).

[20] B. De Neeve, T.-L. Nguyen, T. Behrle, and J. P. Home, Error correction of a logical grid state qubit by dissipative pumping, Nat. Phys. **18**, 296 (2022).

[21] V. G. Matsos, C. H. Valahu, T. Navickas, A. D. Rao, M. J. Millican, X. C. Kolesnikow, M. J. Biercuk, and T. R. Tan, Robust and deterministic preparation of bosonic logical states in a trapped ion, Phys. Rev. Lett. **133**, 050602 (2024).

[22] V. G. Matsos, C. H. Valahu, M. J. Millican, T. Navickas, X. C. Kolesnikow, M. J. Biercuk, and T. R. Tan, Universal quantum gate set for Gottesman-Kitaev-Preskill logical qubits, Nat. Phys., **21**, 1664 (2005).

[23] S. Konno, W. Asavanant, F. Hanamura, H. Nagayoshi, K. Fukui, A. Sakaguchi, R. Ide, F. China, M. Yabuno, S. Miki, *et al.*, Logical states for fault-tolerant quantum computation with propagating light, Science **383**, 289 (2024).

[24] M. H. Michael, M. Silveri, R. T. Brierley, V. V. Albert, J. Salmilehto, L. Jiang, and S. M. Girvin, New class of quantum error-correcting codes for a bosonic mode, Phys. Rev. X **6**, 031006 (2016).

[25] T. Hillmann, F. Quijandría, A. L. Grimsmo, and G. Ferrini, Performance of teleportation-based error-correction circuits for

bosonic codes with noisy measurements, PRX Quantum **3**, 020334 (2022).
[26] P. Leviant, Q. Xu, L. Jiang, and S. Rosenblum, Quantum capacity and codes for the bosonic loss-dephasing channel, Quantum **6**, 821 (2022).
[27] A. L. Grimsmo, J. Combes, and B. Q. Baragiola, Quantum computing with rotation-symmetric bosonic codes, Phys. Rev. X **10**, 011058 (2020).
[28] Y. Ouyang and E. T. Campbell, Trade-offs on number and phase shift resilience in bosonic quantum codes, IEEE Trans. Inf. Theory **67**, 6644 (2021).
[29] S. Schlör, J. Lisenfeld, C. Müller, A. Bilmes, A. Schneider, D. P. Pappas, A. V. Ustinov, and M. Weides, Correlating decoherence in transmon qubits: Low frequency noise by single fluctuators, Phys. Rev. Lett. **123**, 190502 (2019).
[30] J. J. Burnett, A. Bengtsson, M. Scigliuzzo, D. Niepce, M. Kudra, P. Delsing, and J. Bylander, Decoherence benchmarking of superconducting qubits, npj Quantum Inf. **5**, 54 (2019).
[31] S. E. de Graaf, L. Faoro, J. Burnett, A. A. Adamyan, A. Y. Tzalenchuk, S. E. Kubatkin, T. Lindström, and A. V. Danilov, Suppression of low-frequency charge noise in superconducting resonators by surface spin desorption, Nat. Commun. **9**, 1143 (2018).
[32] J. Lisenfeld, A. Bilmes, A. Megrant, R. Barends, J. Kelly, P. Klimov, G. Weiss, J. M. Martinis, and A. V. Ustinov, Electric field spectroscopy of material defects in transmon qubits, npj Quantum Inf. **5**, 105 (2019).
[33] S. E. de Graaf, L. Faoro, L. B. Ioffe, S. Mahashabde, J. J. Burnett, T. Lindström, S. E. Kubatkin, A. V. Danilov, and A. Y. Tzalenchuk, Two-level systems in superconducting quantum devices due to trapped quasiparticles, Sci. Adv. **6**, eabc5055 (2020).
[34] D. Niepce, J. J. Burnett, M. Kudra, J. H. Cole, and J. Bylander, Stability of superconducting resonators: Motional narrowing and the role of Landau-Zener driving of two-level defects, Sci. Adv. **7**, eabh0462 (2021).
[35] R. W. Simmonds, K. M. Lang, D. A. Hite, S. Nam, D. P. Pappas, and J. M. Martinis, Decoherence in Josephson phase qubits from junction resonators, Phys. Rev. Lett. **93**, 077003 (2004).
[36] O. Astafiev, Y. A. Pashkin, Y. Nakamura, T. Yamamoto, and J. S. Tsai, Quantum noise in the Josephson charge qubit, Phys. Rev. Lett. **93**, 267007 (2004).
[37] R. H. Koch, D. P. DiVincenzo, and J. Clarke, Model for $1/f$ flux noise in SQUIDs and qubits, Phys. Rev. Lett. **98**, 267003 (2007).
[38] B. Altshuler, V. Tognetti, and A. Tagliacozzo, *Quantum Phenomena in Mesoscopic Systems* (IOS Press, Amsterdam, Netherlands, 2003), Vol. 151.
[39] J. Bergli, Y. M. Galperin, and B. L. Altshuler, Decoherence of a qubit by non-Gaussian noise at an arbitrary working point, Phys. Rev. B **74**, 024509 (2006).
[40] J. Bergli, Y. M. Galperin, and B. L. Altshuler, Decoherence in qubits due to low-frequency noise, New J. Phys. **11**, 025002 (2009).
[41] J. Schriefl, Y. Makhlin, A. Shnirman, and G. Schön, Decoherence from ensembles of two-level fluctuators, New J. Phys. **8**, 1 (2006).
[42] C. Müller, J. H. Cole, and J. Lisenfeld, Towards understanding two-level-systems in amorphous solids: Insights from quantum circuits, Rep. Prog. Phys. **82**, 124501 (2019).
[43] D. Biswas, S. Utagi, and P. Mandayam, Noise-adapted quantum error correction for non-Markovian noise Phys. Rev. A **111**, 052413 (2025).
[44] J. F. Kam, S. Gicev, K. Modi, A. Southwell, and M. Usman, Detrimental non-Markovian errors for surface code memory Quantum Sci. Technol. **10**, 035060 (2025).
[45] R. Vasile, S. Maniscalco, M. G. A. Paris, H.-P. Breuer, and J. Piilo, Quantifying non-Markovianity of continuous-variable Gaussian dynamical maps, Phys. Rev. A **84**, 052118 (2011).
[46] G. Torre, W. Roga, and F. Illuminati, Non-Markovianity of Gaussian channels, Phys. Rev. Lett. **115**, 070401 (2015).
[47] E.-M. Laine, J. Piilo, and H.-P. Breuer, Measure for the non-Markovianity of quantum processes, Phys. Rev. A **81**, 062115 (2010).
[48] F. Settimo, H.-P. Breuer, and B. Vacchini, Entropic and trace-distance-based measures of non-Markovianity, Phys. Rev. A **106**, 042212 (2022).
[49] J. Johansson, P. Nation, and F. Nori, Qutip 2: A Python framework for the dynamics of open quantum systems, Comput. Phys. Commun. **184**, 1234 (2013).
[50] J. Johansson, P. Nation, and F. Nori, Qutip: An open-source Python framework for the dynamics of open quantum systems, Comput. Phys. Commun. **183**, 1760 (2012).
[51] H. J. Wold, H. Brox, Y. M. Galperin, and J. Bergli, Decoherence of a qubit due to either a quantum fluctuator, or classical telegraph noise, Phys. Rev. B **86**, 205404 (2012).
[52] I. Lerner, B. Altshuler, and Y. Gefen, *Fundamental Problems of Mesoscopic Physics* (Springer, Dordrecht, 2004).
[53] C. Benedetti, F. Buscemi, P. Bordone, and M. G. A. Paris, Dynamics of quantum correlations in colored-noise environments, Phys. Rev. A **87**, 052328 (2013).
[54] D. Zhou, A. Lang, and R. Joynt, Disentanglement and decoherence from classical non-Markovian noise: Random telegraph noise, Quantum Info. Proc. **9**, 727 (2010).
[55] X. Cai, Quantum dephasing induced by non-Markovian random telegraph noise, Sci. Rep. **10**, 88 (2020).
[56] J. Naikoo, S. Dutta, and S. Banerjee, Facets of quantum information under non-Markovian evolution, Phys. Rev. A **99**, 042128 (2019).
[57] C. Benedetti, M. G. A. Paris, and S. Maniscalco, Non-Markovianity of colored noisy channels, Phys. Rev. A **89**, 012114 (2014).
[58] I. V. Lerner, B. L. Altshuler, and Y. Gefen, *Fundamental Problems of Mesoscopic Physics Interactions and Decoherence* (Springer, Dordrecht, 2004).
[59] E. Paladino, Y. M. Galperin, G. Falci, and B. L. Altshuler, **1/f** noise: Implications for solid-state quantum information, Rev. Mod. Phys. **86**, 361 (2014).
[60] J. Burnett, *et al.*, Evidence for interacting two-level systems from the 1/f noise of a superconducting resonator, Nat. Commun. **5**, 4119 (2014).
[61] A. Serafini, *Quantum Continuous Variables* (CRC Press, London, England, 2023).
[62] G. Torre and F. Illuminati, Exact non-Markovian dynamics of Gaussian quantum channels: Finite-time and asymptotic regimes, Phys. Rev. A **98**, 012124 (2018).
[63] M. F. Richter, R. Wiedenmann, and H.-P. Breuer, Witnessing non-Markovianity by quantum quasi-probability distributions, New J. Phys. **24**, 123022 (2022).

[64] H.-P. Breuer, E.-M. Laine, J. Piilo, and B. Vacchini, *Colloquium*: Non-Markovian dynamics in open quantum systems, Rev. Mod. Phys. **88**, 021002 (2016).

[65] G. Amato, H.-P. Breuer, and B. Vacchini, Generalized trace distance approach to quantum non-Markovianity and detection of initial correlations, Phys. Rev. A **98**, 012120 (2018).

[66] A. G. Dijkstra and Y. Tanimura, Non-Markovianity: Initial correlations and nonlinear optical measurements, Philos. Trans. A Math. Phys. Eng. Sci. **370**, 3658 (2012).

[67] S. Endo, Y. Suzuki, K. Tsubouchi, R. Asaoka, K. Yamamoto, Y. Matsuzaki, and Y. Tokunaga, Quantum error mitigation for rotation symmetric bosonic codes with symmetry expansion Phys. Rev. A **111**, 062402 (2025).

[68] V. V. Albert, K. Noh, K. Duivenvoorden, D. J. Young, R. T. Brierley, P. Reinhold, C. Vuillot, L. Li, C. Shen, S. M. Girvin, B. M. Terhal, and L. Jiang, Performance and structure of single-mode bosonic codes, Phys. Rev. A **97**, 032346 (2018).

[69] U. Leonhardt, J. A. Vaccaro, B. Böhmer, and H. Paul, Canonical and measured phase distributions, Phys. Rev. A **51**, 84 (1995).

[70] H. M. Wiseman and R. B. Killip, Adaptive single-shot phase measurements: The full quantum theory, Phys. Rev. A **57**, 2169 (1998).

[71] H. M. Wiseman and R. B. Killip, Adaptive single-shot phase measurements: A semiclassical approach, Phys. Rev. A **56**, 944 (1997).

[72] M. A. Nielsen, A simple formula for the average gate fidelity of a quantum dynamical operation, Phys. Lett. A **303**, 249 (2002).

[73] A. Y. Kitaev, Quantum computations: Algorithms and error correction, Russ. Math. Surv. **52**, 1191 (1997).

[74] J. Watrous, Semidefinite programs for completely bounded norms, Theory Comput. **5**, 217 (2009).

[75] G. Gutoski, On a measure of distance for quantum strategies, J. Math. Phys. **53**, 032202 (2012).

[76] M. A. Nielsen and I. L. Chuang, *Quantum Computation and Quantum Information: 10th Anniversary Edition* (Cambridge University Press, United States of America, 2010).

[77] G. Chiribella, G. M. D'Ariano, and P. Perinotti, Quantum circuit architecture, Phys. Rev. Lett. **101**, 060401 (2008).

[78] F. Caruso, V. Giovannetti, C. Lupo, and S. Mancini, Quantum channels and memory effects, Rev. Mod. Phys. **86**, 1203 (2014).

[79] T. McCourt, C. Neill, K. Lee, C. Quintana, Y. Chen, J. Kelly, J. Marshall, V. N. Smelyanskiy, M. I. Dykman, A. Korotkov, I. L. Chuang, and A. G. Petukhov, Learning noise via dynamical decoupling of entangled qubits, Phys. Rev. A **107**, 052610 (2023).

[80] M. Abramowitz and I. A. Stegun, *Handbook of Mathematical Functions with Formulas, Graphs, and Mathematical Tables* (Dover, New York, 1964). Also see scipy.python.

[81] https://docs.scipy.org/doc/scipy/reference/generated/scipy.special.exp1.html#scipy.special.exp1.

[82] A. Kenfack and K. Życzkowski, Negativity of the Wigner function as an indicator of non-classicality, J. Opt. B: Quantum Semiclassical Opt. **6**, 396 (2004).

[83] F. Siyouri, M. El Baz, and Y. Hassouni, The negativity of Wigner function as a measure of quantum correlations, Quantum Info. Proc. **15**, 4237 (2016).

[84] I. I. Arkhipov, A. Barasiński, and J. Svozilík, Negativity volume of the generalized Wigner function as an entanglement witness for hybrid bipartite states, Sci. Rep. **8**, 16955 (2018).

[85] J. Lalita, K. G. Paulson, and S. Banerjee, Harnessing quantumness of states using discrete Wigner functions under non-Markovian quantum channels, Ann. Phys. **535**, 2300139 (2023).

[86] F. Siyouri, Markovian and non-Markovian dynamics of nonclassical correlations and Wigner function for GHZ-type coherent states, Int. J. Theor. Phys. **58**, 103 (2019).

[87] J. Svozilík, R. Hidalgo-Sacoto, and I. I. Arkhipov, Universal non-Markovianity detection in hybrid open quantum systems, Sci. Rep. **10**, 18258 (2020).

[88] The definition of the code word $|1\rangle_{N,K}$ has a typo in Ref. [27], which has been corrected here.

[89] Z. He, J. Zou, L. Li, and B. Shao, Effective method of calculating the non-Markovianity $\mathcal{N}$ for single-channel open systems, Phys. Rev. A **83**, 012108 (2011).